# Computing Rates and Distributions of Rock Recovery in Subduction Zones

**Journal Article**

**Author(s):**
Kerswell, Buchanan C.; Kohn, Matthew J.; Gerya, Taras V.

# Geochemistry, Geophysics, Geosystems®

**Author Contributions:**
**Conceptualization:** Buchanan C. Kerswell, Matthew J. Kohn, Taras V. Gerya
**Data curation:** Buchanan C. Kerswell
**Formal analysis:** Buchanan C. Kerswell
**Funding acquisition:** Matthew J. Kohn
**Investigation:** Buchanan C. Kerswell

# Computing Rates and Distributions of Rock Recovery in Subduction Zones

**Buchanan C. Kerswell**[1,2] , **Matthew J. Kohn**[1] , and **Taras V. Gerya**[3]

[1]Department of Geosciences, Boise State University, Boise, ID, USA, [2]Department of Geology & Environmental Earth Science, Miami University, Oxford, OH, USA, [3]Department of Earth Sciences, ETH-Zurich, Zurich, Switzerland

**Abstract** Bodies of rock that are detached (recovered) from subducting oceanic plates, and exhumed to Earth's surface, become invaluable records of the mechanical and chemical processing of rock along subduction interfaces. Exposures of interface rocks with high-pressure (HP) mineral assemblages provide insights into the nature of rock recovery, yet various inconsistencies arise when directly comparing the rock record with numerical simulations of subduction. Constraining recovery rates and depths from the rock record presents a major challenge because small sample sizes of HP rocks reduce statistical power. As an alternative approach, this study implements a classification algorithm to identify rock recovery in numerical simulations of oceanic-continental convergence. Over one million markers are classified from 64 simulations representing a large range of subduction zones. Recovery pressures (depths) correlate strongly with convergence velocity and moderately with oceanic plate age, while slab-top thermal gradients correlate strongly with oceanic plate age and upper-plate thickness. Recovery rates strongly correlate with upper-plate thickness, yet show no correlation with convergence velocity or oceanic plate age. Likewise, pressure-temperature (PT) distributions of recovered markers vary among numerical experiments and generally show deviations from the rock record that cannot be explained by petrologic uncertainties alone. For example, a significant gap in marker recovery is found near 2 GPa and 550°C, coinciding with the highest frequencies of exhumed HP rocks. Explanations for such a gap in marker recovery include numerical modeling uncertainties, selective sampling of exhumed HP rocks, or natural geodynamic factors not accounted for in numerical experiments.

**Plain Language Summary** Bodies of deeply subducted rock that return to Earth's surface bring up information about the interface between converging tectonic plates within subduction zones, yet the mechanisms that detach rock from the subducting plate are not well-understood. As an alternative to studying natural rock samples, this study implements a machine learning algorithm to identify rock detachment in numerical simulations. Over one million simulated rocks are classified from 64 simulations representing a large range of possible subduction zones. Pressure-temperature (PT) conditions of simulated rocks are compared across models and with the natural rock record. Correlations are drawn among important model parameters that reveal strong and weak effects on detachment of simulated rocks from the subducting plate. Recovery rates strongly correlate with upper-plate thickness, yet show no correlation with other parameters. Likewise, PT distributions of simulated rocks show variable compatibility with the natural rock record depending on the comparison. A significant gap in simulated rock recovery coincides with a large proportion of samples analyzed from the natural rock record. Explanations for such a gap in simulated rock recovery include numerical modeling uncertainties, selective sampling of natural rocks, or geodynamic factors not accounted for in numerical experiments.

## 1. Introduction

Maximum pressure-temperature (PT) conditions have been estimated for hundreds of high-pressure (HP) metamorphic rocks exhumed from subduction zones (Figure 1, Agard et al., 2018; Hacker, 1996; Penniston-Dorland et al., 2015). These samples represent fragments of oceanic crust, continental crust, seafloor sediments, and upper mantle that have detached from subducting oceanic and continental lithospheres at various depths along the interface between subducting and overriding tectonic plates (referred to as "recovery" after Agard et al., 2018). This *rock record* is the only tangible evidence of PT-strain fields, deep seismic cycling, and fluid flow within Earth's lithosphere during deformation and chemical processing in subduction zones. Together with geophysical imaging (e.g., Bostock, 2013; Ferris et al., 2003; Hyndman & Peacock, 2003; Mann et al., 2022; Naif et al., 2015; Rondenay et al., 2008; Syracuse & Abers, 2006), analysis of surface heat flow data (e.g., Currie &

Hyndman, 2006; Gao & Wang, 2014; Hyndman et al., 2005; Kohn et al., 2018; Morishige & Kuwatani, 2020; Wada & Wang, 2009), and forward numerical geodynamic modeling (e.g., Gerya & Stöckhert, 2006; Gerya et al., 2002, 2008; Hacker et al., 2003; Kerswell et al., 2021; McKenzie, 1969; Peacock, 1990, 1996; Sizova et al., 2010; Syracuse et al., 2010; Yamato et al., 2007, 2008), investigation of the rock record underpins contemporary understandings of subduction geodynamics (e.g., Agard, 2021; Agard et al., 2009; Bebout, 2007).

However, it remains difficult to directly interpret the rock record in terms of recovery rates and distributions along the subduction interface. For example, compilations of PT estimates representing the global distribution of HP rocks exhumed during the Phanerozoic (the pd15 and ag18 datasets, Agard et al., 2018; Penniston-Dorland et al., 2015) reveal an abrupt decrease in relative sample abundance at P's above 2.3–2.4 GPa (Figure 1 inset). For pd15 and ag18, a nearly constant cumulative distribution function (CDF) interrupted by a sharp change in slope around 2.3–2.4 GPa implies relatively widespread recovery of subducting material up to 2.3–2.4 GPa, but increasingly rare recovery at higher P (Agard et al., 2018; Kerswell et al., 2021; Kohn et al., 2018; Monié & Agard, 2009; Plunder et al., 2015). On the one hand, evidence for common mechanical coupling depths near 2.3 GPa (Furukawa, 1993; Kerswell et al., 2021; Wada & Wang, 2009) suggests an upper-limit to recovery depths that is consistent with the scarcity of (ultra-)HP samples in the rock record and invariant with respect to key thermo-kinematic parameters (convergence velocity, subduction geometry, plate thickness; Figure 1). On the other hand, geophysical constraints on the depths of key mechanical transitions likely to induce rock recovery (e.g., Abers et al., 2020; Audet & Kim, 2016; Audet & Schaeffer, 2018; Morishige & Kuwatani, 2020) suggest high recovery rates should cluster around discrete depths, rather than widespread recovery along the subduction interface implied by the pd15 and ag18 datasets.

Difficulties in relating complex polymetamorphic rocks from different environments challenge the use of PT distributions of exhumed HP rock samples as robust constraints on key subduction zone parameters. Interpretations of rock recovery mechanisms, subduction interface behavior, metamorphic reactions, seismic cycling, and subduction geodynamics might vary depending on metamorphic terrane (local tectonic environment), sampling strategy (random or targeted outcrops), sample size (how many outcrops were observed and sampled in the field), and analytical sample selection (investigating PT's and deformation histories for a subset of samples with a specific scientific question in mind). Different compilations of PT estimates from natural samples can show different distributions in terms of relative abundances (frequencies) of samples across PT space, and thus imply a natural preference of rock recovery (and/or exhumation) from different depths along the subduction interface. For example, Agard et al. (2018) noted that compilations from Plunder et al. (2015) and Groppo et al. (2016) show less dispersion (i.e., a more step-like CDF) than ag18 with tighter bimodal or trimodal distributions clustering around inferred depths of important mechanical transitions along the subduction interface. That is, high-frequency peaks (modes) in PT distributions of exhumed HP rocks are inferred to coincide with the continental Moho at approximately 25–35 km and the transition to mechanical plate coupling at approximately 80 km (Agard et al., 2018; Monié & Agard, 2009; Plunder et al., 2015). Less attention in the literature is paid to a smaller, yet significant, intermediate mode at 55–60 km (Agard et al., 2009, 2018; Plunder et al., 2015), although it is consistent with a high-frequency region of PT estimates in the pd15 data set.

Differences in compiled PT datasets notwithstanding, key observations regarding rock recovery in subduction zones emerge from pd15 and ag18:

**Pressure**

- Rock recovery is broadly and unequally distributed
- Rock recovery is more frequent near 1 and 2 GPa (bimodal)
- 64%–66% of recovered rocks equilibrated between 1 and 2.5 GPa
- 5%–19% of recovered rocks equilibrated above 2.5 GPa

**Temperature**

- 50%–56% of recovered rocks equilibrated above 525°C
- 32%–34% of recovered rocks equilibrated between 350 and 525°C

**PT gradient**

- 52%–62% of recovered rocks record gradients between 5 and 10°C/km
- 18%–31% of recovered rocks record gradients between 10 and 15°C/km
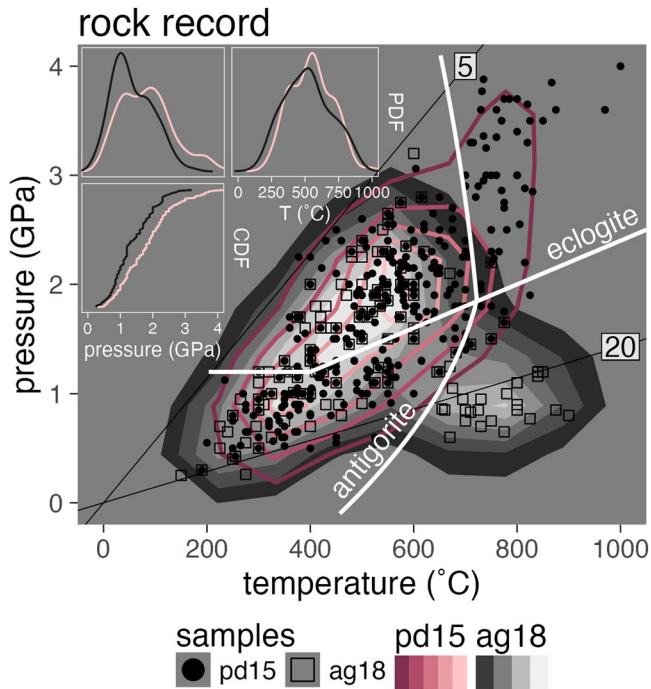
**Figure 1.** Pressure-temperature (PT) diagram showing distributions of PT estimates for exhumed high-pressure metamorphic rock samples compiled in the pd15 (solid contours, Penniston-Dorland et al., 2015) and ag18 (filled contours, Agard et al., 2018) datasets. Thin lines are thermal gradients labeled in °C/km. Reaction boundaries for eclogitization of oceanic crust and antigorite dehydration are from Ito and Kennedy (1971) and Schmidt and Poli (1998), respectively (insets). Probability distribution functions of pd15 (pink lines) and ag18 samples (black lines) showing broad bimodal and trimodal sample distributions with respect to P (top left inset) and a kinked cumulative distribution function (bottom inset) indicating that a substantial proportion of rocks are recovered from P's between 0.5 and 2.5 GPa with very few rocks reaching maximum P's above 3 GPa.

- 6%–30% of recovered rocks record gradients above 15°C/km

These ranges in the relative abundances of exhumed HP rocks compiled in different datasets raise important questions in subduction zone research: are rocks recovered broadly and uniformly along the subduction interface or discretely from certain depths? How do recovery rates and distributions vary among diverse subduction zone settings and through time?

Previous work comparing the rock record directly with numerical models has generally produced ambiguous interpretations concerning recovery rates (the volumetric ratio of recovered:subducted material) and PT distributions of recovery along the subduction interface—especially with respect to P, or depth. For example, comparisons of different numerical geodynamic codes with subsets of the rock record show variable agreement in terms of over-lapping PT paths and thermal gradients (e.g., Angiboust, Wolf, et al., 2012; Burov et al., 2014; Holt & Condit, 2021; Penniston-Dorland et al., 2015; Plunder et al., 2018; Roda et al., 2010, 2012, 2020; Ruh et al., 2015; Yamato et al., 2007, 2008). Numerous factors potentially contribute to inconsistent PT distributions and thermal gradients between exhumed HP rocks and numerical geodynamic models, including initial setups for numerical experiments and ranges in thermo-kinematic boundary conditions (i.e., subduction zone setting: oceanic plate age, convergence velocity, subduction dip angle, upper-plate thickness, and heating sources; Kohn et al., 2018; Penniston-Dorland et al., 2015; Ruh et al., 2015; van Keken et al., 2019), differential recovery rates from subduction zones with favorable settings (Abers et al., 2017; van Keken et al., 2018), and comparisons among suites of undifferentiated HP rocks (e.g., grouping rocks recovered during subduction initiation with rocks recovered during "steady-state" subduction, see Agard et al., 2018, 2020). Compounding the ambiguity are arguments that material is sporadically recovered during short-lived mechanical transitions (Agard et al., 2016) and/or geodynamic changes (Monié & Agard, 2009)—implying exhumed HP rocks are not random samples of the subduction interface during steady-state subduction. Such ambiguities warrant further investigation into the general response of recovery rates and distributions to broad ranges of subduction zone settings and various implementations of subduction interface rheologies.

Fortunately, clues about the nature and PT limits of rock recovery are provided by many extensively studied examples of exhumed subduction interfaces (e.g., Agard et al., 2018; Angiboust et al., 2011, 2015; Cloos & Shreve, 1988; Fisher et al., 2021; Ioannidi et al., 2020; Kitamura & Kimura, 2012; Kotowski & Behr, 2019; Locatelli et al., 2019; Monié & Agard, 2009; Okay, 1989; Platt, 1986; Plunder et al., 2013, 2015; Tewksbury-Christle et al., 2021; Wakabayashi, 2015). However, these type localities represent an unknown fraction of subducted material and differ significantly in terms of their geometry (field relationships), composition (rock types), and interpreted deformation histories (both detachment and exhumation). It is also unclear to what extent ag18 and pd15 (and other compilations) represent the full range of recovery conditions and/or represent scientific sampling bias (e.g., undersampling low-grade rocks or oversampling high-grade rocks from the same pristine exposures, Agard et al., 2018) or other geodynamic biases (e.g., preferential exhumation, Abers et al., 2017; van Keken et al., 2018). Thus, a primary challenge to inferring recovery rates and distributions accurately from the rock record fundamentally stems from sparse nonrandom samples (typically less than a few dozen PT estimates from any given exhumed terrane) compared to the diversity of thermo-kinematic parameters characterizing subduction zones and dynamic petro-thermo-mechanical processes that might trigger rock recovery along the subduction interface.

This study aims at addressing the sparsity and nonrandomness of exhumed HP rock samples by tracing numerous (1,341,729) Lagrangian markers from 64 numerical geodynamic simulations of oceanic-continental subduction (Kerswell et al., 2021). We first generate a PT data set from instantiations of a particular numerical geodynamic

code so large that it was insensitive to noise and outliers—thus representing a statistically robust picture of recovery rates and PT distributions of recovery in subduction zone models. From such a large data set of generated samples, we identify correlations among recovery rates, PT distributions, and subduction zone settings (i.e., oceanic plate age, convergence velocity, and upper-plate thickness) that test sensitivities and indicate ranges of plausible conditions for reproducing the rock record. In fact, numerical experiments predict surprisingly few recovered samples corresponding with the PT region around 2 GPa and 550°C—the same PT region that has a relatively high-frequency of natural samples. We then discuss implications for inconsistencies between frequencies of generated samples and exhumed HP rocks, including insufficient implementation of recovery mechanisms in numerical geodynamic models (numerical bias), a potential overabundance of natural samples collected from similar metamorphic grades around 2 GPa and 550°C (sampling bias), and preferential exhumation from a relatively narrow range of PT conditions (geodynamic bias).

## 2. Methods

This study presents a data set of Lagrangian markers (described below) from numerical experiments that simulated 64 oceanic-continental convergent margins with thermo-kinematic boundary conditions (oceanic plate age, convergence velocity, and upper-plate lithospheric thickness) closely representing the range of presently active subduction zone settings (Syracuse & Abers, 2006; Wada & Wang, 2009). Initial conditions were modified from previous studies of active margins (Gorczyk et al., 2007; Sizova et al., 2010) using the numerical geodynamic code I2VIS (Gerya & Yuen, 2003), which models visco-plastic flow of geological materials by solving conservative equations of mass, energy, and momentum on a fully staggered finite difference grid with a *marker-in-cell* technique (e.g., Gerya, 2019; Gerya & Yuen, 2003; Harlow & Welch, 1965). Complete details about the initial setup, boundary conditions, and rheological model are presented in Kerswell et al. (2021). Complete details about I2VIS and example code are presented in Gerya and Yuen (2003) and Gerya (2019).

The following section summarizes the numerical modeling setup, then defines Lagrangian markers (now referred to as *markers*) and briefly elaborates on their usefulness in understanding flow of geological materials, followed finally by a description of the marker classification algorithm. A complete mathematical description of the classification algorithm is presented in Appendix A1.

### 2.1. Summary of the Numerical Modeling Setup

The numerical geodynamic models of Kerswell et al. (2021) used for generating the markers data set in this study are 2,000 km wide and 300 km deep with nonuniform resolution that increases gradually from $5 \times 1$ km at the boundaries (in the *x*- and *z*-directions, respectively) to $1 \times 1$ km within a 600 km wide area surrounding the contact between the oceanic plate and continental margin. The left and right boundaries are free-slip and thermally insulating. "Sticky" air and water at the top boundary allow for a free topographical surface with a simple linear implementation of sedimentation and erosion. The lower boundary is open to allow for free subduction geometries during oceanic plate descent (Burg & Gerya, 2005).

#### 2.1.1. Rheological Model

All rock types within the model domain are treated as visco-plastic materials by limiting diffusion and dislocation creep deformation mechanisms with a brittle (plastic) yield criterion. Contributions from dislocation and diffusion creep are accounted for by computing a composite rheology for ductile rocks, $\eta_{eff}$:

$$\frac{1}{\eta_{eff}} = \frac{1}{\eta_{diff}} + \frac{1}{\eta_{disl}}$$

(1)

where $\eta_{diff}$ and $\eta_{disl}$ are effective viscosities for diffusion and dislocation creep.

**Table 1**
*Material Properties Used in Numerical Experiments*

| Material | $\rho$ (kg/m³) | $H_2O$ (wt.%) | Flow law | $log_{10}A$ | $E$ (kJ/mol) | $V$ (J/MPa·mol) | $n$ | $\phi$ | $\sigma_{crit}$ (MPa) | $k_1$ | $k_2$ | $k_3$ | $H$ (µW/m³) |
|---|---|---|---|---|---|---|---|---|---|---|---|---|---|
| Sediments | 2,600 | 5.0 | Wet quartzite | −3.5 | 154.0 | 3.0 | 2.3 | 0.15 | 0.03 | 0.64 | 807 | 4e−06 | 2.000 |
| Felsic crust | 2,700 | | Wet quartzite | −3.5 | 154.0 | 3.0 | 2.3 | 0.45 | 0.03 | 0.64 | 807 | 4e−06 | 1.000 |
| Basalt | 3,000 | 5.0 | Plag an75 | −3.5 | 238.0 | 8.0 | 3.2 | 0.45 | 0.03 | 1.18 | 474 | 4e−06 | 0.250 |
| Gabbro | 3,000 | | Plag an75 | −3.5 | 238.0 | 8.0 | 3.2 | 0.45 | 0.03 | 1.18 | 474 | 4e−06 | 0.250 |
| Mantle dry | 3,300 | | Dry olivine | 4.4 | 540.0 | 20.0 | 3.5 | 0.45 | 0.30 | 0.73 | 1,293 | 4e−06 | 0.022 |
| Mantle hydrated | 3,300 | 0.5 | Wet olivine | 3.3 | 430.0 | 10.0 | 3.0 | 0.45 | 0.24 | 0.73 | 1,293 | 4e−06 | 0.022 |
| Serpentine | 3,200 | 2.0 | Serpentine | 3.3 | 8.9 | 3.2 | 3.8 | 0.15 | 3.00 | 0.73 | 1,293 | 4e−06 | 0.022 |

*Note.* Key: A: material constant, E, V: activation energy and volume, n: power law exponent, $\phi$: internal friction angle, $\sigma_{crit}$: critical stress, $k_1$–$k_3$: thermal conductivity constants, H: heat production. Constants: $C_p$: heat capacity = 1 [kJ/kg], $\alpha$: expansivity = $2 \times 10^{-5}$ [1/K], $\beta$: compressibility = $2 \times 10^{-5}$ [1/MPa]. Thermal conductivity: $k$ [W/mK] = $\left(k_1 + \frac{k_2}{T+77}\right) \times \exp(k_3 \cdot P)$ with $P$ in [MPa] and $T$ in [K]. References: Turcotte and Schubert (2002), Ranalli (1995), Hilairet et al. (2007), and Karato and Wu (1993).

For the crust and serpentinized mantle, $\eta_{diff}$ and $\eta_{disl}$ are computed as:

$$\begin{aligned} \eta_{diff} &= \frac{1}{2} A \, \sigma_{crit}^{1-n} \exp\left[\frac{E + PV}{RT}\right] \\ \eta_{disl} &= \frac{1}{2} A^{1/n} \, \dot{\varepsilon}_{II}^{(1-n)/n} \exp\left[\frac{E + PV}{nRT}\right] \end{aligned} \quad (2)$$

where $R$ is the gas constant, $P$ is pressure, $T$ is temperature in $K$, $\dot{\varepsilon}_{II} = \sqrt{\frac{1}{2}\dot{\varepsilon}_{ij}^2}$ is the square root of the second invariant of the strain rate tensor, $\sigma_{crit}$ is an assumed diffusion-dislocation transition stress, and $A$, $E$, $V$ and $n$ are the material constant, activation energy, activation volume, and stress exponent, respectively (Table 1, Hilairet et al., 2007; Ranalli, 1995).

For the mantle, $\eta_{diff}$ and $\eta_{disl}$ are computed as (Karato & Wu, 1993):

$$\begin{aligned} \eta_{diff} &= \frac{1}{2} A^{-1} G \left[\frac{h}{b}\right]^{m/n} \exp\left[\frac{E + PV}{RT}\right] \\ \eta_{disl} &= \frac{1}{2} A^{-1/n} G \, \dot{\varepsilon}_{II}^{(1-n)/n} \exp\left[\frac{E + PV}{nRT}\right] \end{aligned} \quad (3)$$

where $b = 5 \times 10^{-10}$ m is the Burgers vector, $G = 8 \times 10^{10}$ Pa is shear modulus, $h = 1 \times 10^{-3}$ m is the assumed grain size, $m = 2.5$ is the grain size exponent, and the other flow law parameters are given in Table 1. Viscosity is limited in all numerical experiments from $\eta_{min} = 10^{17}$ Pa · s to $\eta_{max} = 10^{25}$ Pa · s.

An effective visco-plastic rheology is achieved by limiting $\eta_{eff}$ with a brittle (plastic) yield criterion:

$$\eta_{eff} \leq \frac{C + \phi P}{2 \, \dot{\varepsilon}_{II}} \quad (4)$$

where $\phi$ is the internal friction coefficient, $C$ cohesive strength at $P = 0$, and $\dot{\varepsilon}_{ij}$ is the strain rate tensor (Table 1).

### 2.1.2. Metamorphic (De)hydration Reactions

Within the model domain, free water particles are generated and consumed by empirically derived (de)hydration reactions and migrate with relative velocities defined by local deviatoric (non-lithostatic) pressure gradients (Faccenda et al., 2009). In the subducting lithosphere, gradual eclogitization of oceanic crust is computed as a linear function of lithostatic pressure. This effectively simulates continuous influx of water to the upper-plate mantle beginning with compaction and release of connate water at shallow depths, followed by a sequence of reactions consuming major hydrous phases (chlorite, lawsonite, zoisite, chloritoid, talc, amphibole, and phengite) in different parts of the hydrated basaltic crust (Schmidt & Poli, 1998; van Keken et al., 2011). Besides gradual water release, eclogitization of the oceanic crust involves densification at the garnet-in and plagioclase-out reaction boundaries defined by Ito and Kennedy (1971).

In the upper-plate mantle wedge, formation of brucite and serpentine from dry olivine is inferred to strongly regulate mechanical behavior of the plate interface (Agard et al., 2016; Hyndman & Peacock, 2003; Peacock & Hyndman, 1999). Because brucite breaks down at much lower temperatures than serpentine (e.g., Bowen & Tuttle, 1949; Schmidt & Poli, 1998), serpentine (de)stabilization is arguably more responsible for regulating interface rheology deep in subduction zones. Thus, Kerswell et al. (2021) chose to explicitly model serpentine (de)hydration in the upper mantle, which effectively induces a mechanical (de)coupling transition at the *antigorite ⇔ olivine + orthopyroxene + H₂O* reaction boundary defined by Schmidt and Poli (1998). All such (de)hydration reactions tacitly assume thermodynamic equilibrium.

## 2.2. Lagrangian Markers

Markers are mathematical objects representing discrete parcels of material flowing in a continuum (Harlow, 1962, 1964). Tracing markers (saving marker information at each timestep) advances the investigation of subduction dynamics in the following two ways.

First, modeling subduction requires solving equations of mass, motion, and heat transport in a partly layered, partly heterogeneous, high-strain region known as the *plate interface*, *subduction interface*, or *subduction channel* (Gerya et al., 2002). Current conceptual models regard the subduction interface as a visco-plastic continuum with complex geometry and structure, sharp thermal, chemical, and strain gradients, strong advection, and abundant fluid flow (Agard et al., 2016, 2018; Bebout, 2007; Bebout & Barton, 2002; Cloos & Shreve, 1988; Gerya & Yuen, 2003; Shreve & Cloos, 1986; Stöckhert, 2002; Tewksbury-Christle et al., 2021). Finite-difference numerical approaches do not perform well with strong local gradients, and interpolating and updating T, strain, and chemical fields with markers greatly improves accuracy and stability of numerical solutions (Gerya, 2019; Gerya & Yuen, 2003; Moresi et al., 2003).

Second, tracing a marker closely proxies for tracing a rock's PT-time history. Strictly speaking, deviations between calculated PT-time histories of markers and rocks are possible because the numerical geodynamic simulations assume: (a) markers move in an incompressible continuum (Batchelor, 1953; Boussinesq, 1897), (b) material properties are governed by a simplified petrologic model describing eclogitization of oceanic crust (Ito & Kennedy, 1971) and (de)hydration of upper mantle (*antigorite* ⇔ *olivine* + *orthopyroxene* + $H_2O$, Schmidt & Poli, 1998), and (c) marker stress and strain are related by a highly non-linear rheological model derived from empirical flow laws (Hilairet et al., 2007; Karato & Wu, 1993; Ranalli, 1995; Turcotte & Schubert, 2002). For example, if rocks within a subduction interface shear zone were highly compressible or could sustain large deviatoric stresses, P's and T's might be different from markers.

The rheological model implemented in the numerical simulations of Kerswell et al. (2021), embodied by assumptions 2 and 3, exert particularly strong control on subduction interface strength, and thus the probability and style of detachment. For example, all numerical simulations from Kerswell et al. (2021) developed stable subduction channels (tectonic-mélanges, e.g., Gerya et al., 2002) instead of discrete shear zones that detach large coherent slices of oceanic lithosphere (e.g., Ruh et al., 2015) primarily due to the choice of rheological model and specific implementation of metamorphic (de)hydration reactions. A major uncertainty in the markers data set presented below stems from an implicit assumption that the plate interface behaves like a distributed shear zone composed of hydrated ultramafic material mixed with fragments of dehydrating oceanic crust and seafloor sediments (i.e., a tectonic mélange). Field evidence for tectonic slicing of HP rocks does not necessarily support this view of plate interface behavior (e.g., Agard et al., 2018; Angiboust et al., 2009, 2014; Angiboust, Langdon, et al., 2012; Gilio et al., 2020; Locatelli et al., 2018; Monié & Agard, 2009; Poulaki et al., 2023), while other well-studied mélange-like structures do (e.g., Festa et al., 2019; Harvey et al., 2021; Hsü, 1968; Kusky et al., 2013; Penniston-Dorland & Harvey, 2023; Platt, 2015; Wakabayashi & Dilek, 2011), and still other localities exhibit field relations that are more ambiguous (e.g., Bonnet et al., 2018; Cisneros et al., 2022; Kotowski et al., 2022; Kusky et al., 2013; Platt, 1975). Such a variety of different structures interpreted as former plate interfaces highlight the fact that large uncertainties exist in the rock record—in addition to large experimental and theoretical uncertainties—all of which challenge our understanding of plate interface mechanics in subduction zones. Large uncertainties notwithstanding, our objective was to assess the rates and PT distribution of HP rock recovery during steady state subduction in a distributed shear zone, not necessarily during short-lived events that might induce tectonic slicing of subducting lithosphere. Therefore, insofar as the plate interface approximates a mélange-like channel of incompressible visco-plastic fluid (under the assumptions above, Gerya, 2019; Gerya & Yuen, 2003; Kerswell et al., 2021), first-order comparisons between marker PT distributions and the rock record may be made.

## 2.3. Marker Classification

For each numerical experiment, 20,986 markers were initially selected from within a 760 km-long and 8 km-deep section of oceanic crust and seafloor sediments at $t = 0$ Ma. Tracing proceeded for 115 timesteps (between 9.3 and 54.7 Ma depending on convergence velocity), which was sufficient for markers to be potentially subducted very deeply (up to 300 km) from their initial positions. To a first-order, however, only markers that detached from the subducting oceanic plate (i.e., not subducted) were relevant for comparison with PT estimates of exhumed

HP rocks. The main challenge, therefore, was to first develop a method for determining which markers among 20,986 detached from the subducting plate without knowing their fate a priori. Moreover, the method needed to be generalizable to a large range of numerical experiments.

Classifying unlabeled markers as either "recovered" or "not recovered" based solely on their undifferentiated traced histories defines an unsupervised classification problem (Barlow, 1989). Many methods can be applied to solve the unsupervised classification problem, yet this study implemented a Gaussian mixture model (Reynolds, 2009)—a type of "soft" clustering algorithm used extensively for pattern recognition, anomaly detection, and estimating complex probability distribution functions (e.g., Banfield & Raftery, 1993; Celeux & Govaert, 1995; Figueiredo & Jain, 2002; Fraley & Raftery, 2002; Vermeesch, 2018). "Hard" classification is possible by directly applying simple rules to markers without clustering (e.g., Roda et al., 2012). However, "hard" methods are less generalizable than "soft" approaches like Gaussian mixture models, which can be implemented to study many possible features in numerical simulations with Lagrangian reference frames—not just recovery of subducted material. In this case, a Gaussian mixture model organized markers into groups (clusters) by fitting $k = 14$ bivariate Gaussian ellipsoids to the distribution of markers in PT space. "Fitting" refers to adjusting parameters (centroids and covariance matrices) of all $k$ Gaussian ellipsoids until the ellipsoids and data achieved maximum likelihood (see Appendix A1 for a complete mathematical description). Finally, marker clusters with centroids located within certain bounds were classified as "recovered." The entire classification algorithm can be summarized as follows:
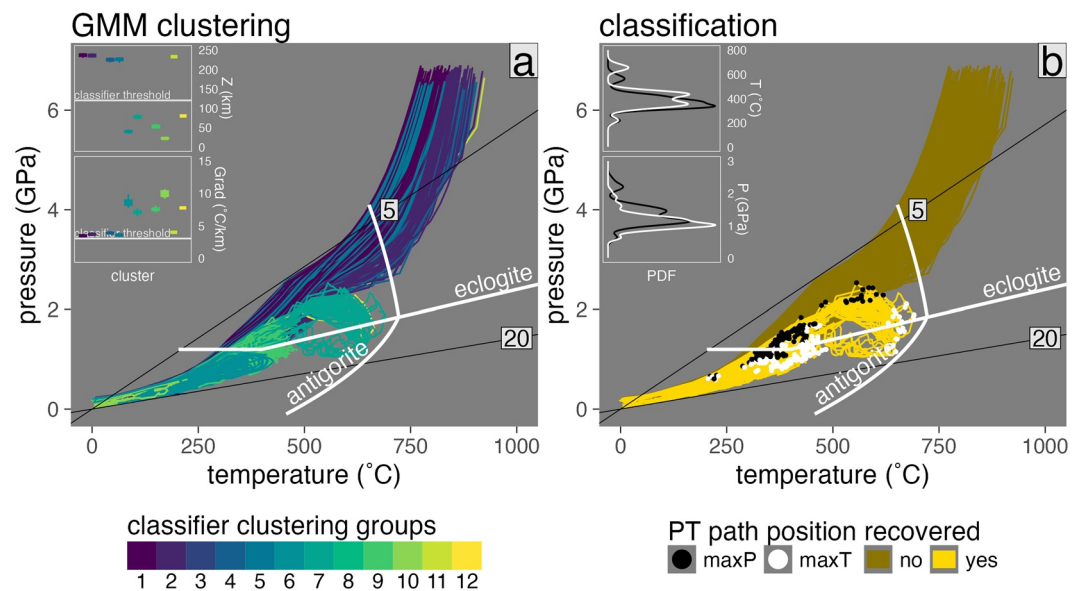
**Marker classification algorithm**

0. Select markers within a 760 km × 8 km section of oceanic crust
1. Trace markers for 115 timesteps
2. Identify maximum marker PT conditions (at [maxP, T] or "maxP")
3. Apply Gaussian mixture modeling to maximum marker PT conditions
4. Check for cluster centroids within the bounds:
   - ≥3°C/km AND
   - ≤1300°C AND
   - ≤120 km (3.4 GPa)
5. Classify marker clusters found in step 4 as "recovered"
6. Classify all other markers as "not recovered"

Note that marker PT's used for clustering were assessed before markers melted. Melting was implemented in the numerical experiments of Kerswell et al. (2021) but was irrelevant for marker clustering. Marker PT's used for clustering were also assessed before the accretionary wedge toe collided with the high-viscosity convergence region positioned at 500 km from the left boundary to avoid spurious PT conditions associated with sudden isothermal burial. We also tested different prograde PT path positions in step 2 by determining maximum marker T's (P, maxT or "maxT") and maximum P's (maxP, T or "maxP") independently. Applying maxP versus maxT conditions to the classifier resulted in distinct PT distributions of recovered markers and correlations with subduction zone settings. However, compilations of exhumed HP rocks emphasize maxP, not maxT (Penniston-Dorland et al., 2015), and thus empirical PT estimates are best compared with maxP conditions. Also, many PT paths for exhumed HP rocks have "hairpin" or isothermal decompression retrograde PT paths without significant heating during exhumation (Agard et al., 2009). Figures 2 and 3 illustrate marker classification for 1 of 64 numerical experiments. All other experiments are presented in Supporting Information S1.

When evaluating the comparisons between markers and rocks made below, it is important that detached markers classified as "recovered" were not exhumed to the surface within the modeling domain. In fact, very few markers exhumed to any significant degree after detachment from the subducting plate. In natural systems, diverse processes drive exhumation of subduction zone rocks, including later tectonic events (Agard et al., 2009). However, our goal was to compare only the maximum metamorphic conditions of markers and rocks along their prograde paths during steady-state subduction. Because most rocks in pd15 and ag18 are inferred to have relatively tight closed-loop PT paths (Agard et al., 2018; Penniston-Dorland et al., 2015), it is reasonable to assume that their maximum PT estimates closely correspond to the point of detachment (recovery) along the plate interface. Therefore, our analysis compared maximum PT estimates for exhumed rocks with PT conditions during marker detachment from the subducting plate.

**Figure 2.** Example of marker classification for model cda62. (a) Pressure-temperature (PT) diagram showing marker clusters as assigned by Gaussian mixture modeling (GMM; colored PT paths). Boxplots showing depth and thermal gradient distributions of marker clusters assigned by GMM. Markers belonging to clusters with centroids (means) positioned at ≤120 km (top inset) and ≥3°C/km (bottom inset) are classified as recovered. All others are classified as not recovered. (b) PT diagram showing marker classification results (colored PT paths) and various marker positions along their PT paths (black, white, and pink points). Thin lines are thermal gradients labeled in °C/km. Only a random subset of markers is shown. (insets) Probability distribution functions showing the distribution of T's (top inset) and P's (bottom inset) for recovered markers at maxP (black lines) and maxT (white lines) conditions. In this experiment, a significant number of markers have different peak metamorphic conditions between their maxT and maxP positions.

## 2.4. Recovery Modes

To better quantify how rock recovery can vary among different subduction zone settings, marker recovery modes (high-frequency peaks) were determined with respect to absolute PT and PT gradients. The highest-frequency peak (mode1) shows where the greatest abundance of markers are recovered. The deepest, or warmest, frequency peak (mode2) shows where the most deeply subducted markers (or markers with the highest PT gradients) are recovered. It is crucial to understand that mode2 represents a very small number of recovered markers compared to mode1 in all cases (typically ≤1%–10%). In other words, changes in the positions of mode1 and mode2 reflect variations in recovery conditions (P, T, and PT gradients) for "normal" recovery and "extreme cases," respectively.

Note that correlations are not presented here with respect to the thermal parameter $\Phi$ ($\Phi$ = oceanic plate age · convergence velocity), unlike other studies (e.g., England et al., 2004; Wada & Wang, 2009). The rationale is three-fold: (a) the aim was to understand how oceanic plate age and convergence velocity affect marker recovery independently, (b) sample sizes of recovered markers were larger when grouped by oceanic plate age and convergence velocity ($n = 335,788$) compared to grouping by $\Phi$ ($n = 83,947$; implying they do not correlate well with $\Phi$), and (c) combining oceanic plate age and convergence velocity can draw unnecessarily ambiguous associations with other geodynamic features of subduction zones (e.g., $\Phi$ vs. $H$ from England et al. (2004) and Wada and Wang (2009)).

## 3. Results

### 3.1. Comparing Marker PT Distributions With the Rock Record

### 3.1.1. Markers From All Numerical Experiments

While marker recovery can occur at all P's recorded by exhumed metamorphic rocks (Figure 4), numerical experiments predict that most markers are recovered from discrete regions (depths) along the plate interface. For
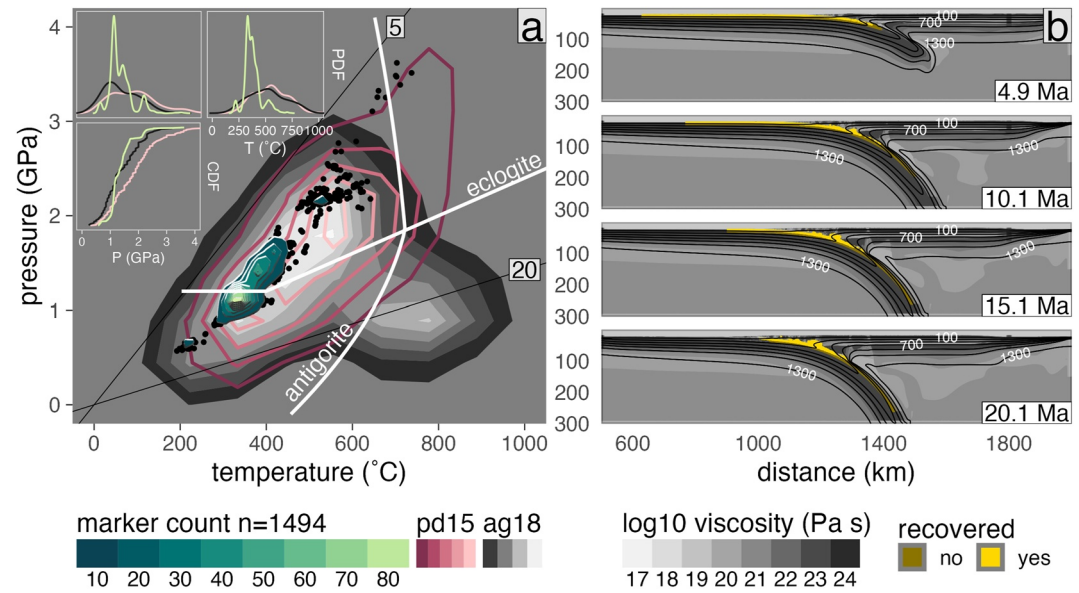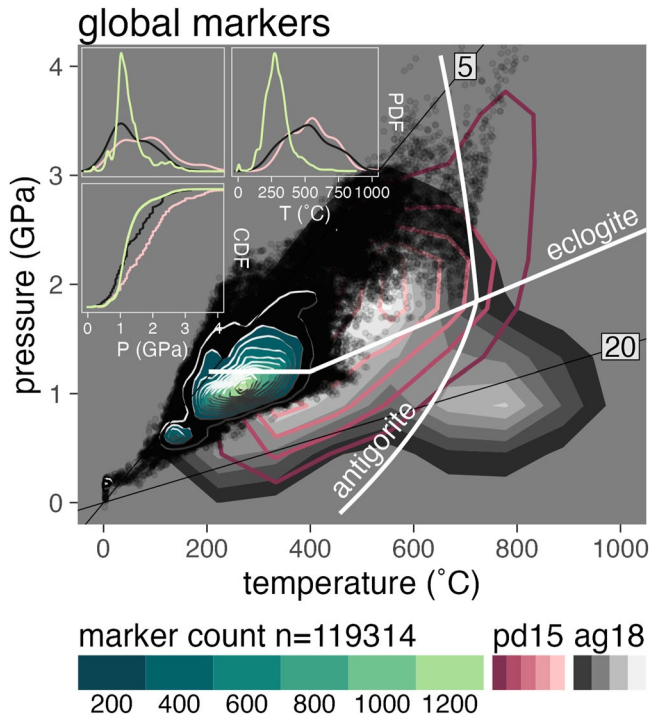
**Figure 3.** Summary of marker recovery for model cda62. (a) Pressure-temperature diagram showing the frequency of recovered markers (black points and green Tanaka contours) in comparison with the pd15 (solid red contours) and ag18 (filled gray contours) data sets. Thin lines are thermal gradients labeled in °C/km. Reaction boundaries for eclogitization of oceanic crust and antigorite dehydration are from Ito and Kennedy (1971) and Schmidt and Poli (1998), respectively. Marker counts (Tanaka contours) are computed across a $100 \times 100$ grid ($0.04$ GPa $\times 10$°C). (insets) Probability distribution functions (top insets) and cumulative distribution functions (bottom inset) comparing P and T distributions between numerical experiments (green lines) and natural samples (pink lines: pd15, black lines: ag18). (b) Visualization of log viscosity in the model domain showing the major modes of marker recovery along a relatively thick subduction interface that tapers near the viscous coupling depth.

example, pd15 and ag18 show high sample frequencies from near 1 GPa—a shared feature common to all 64 numerical experiments. Yet samples recovered from above 1 GPa are much more frequent in pd15 and ag18 compared to simulations (relative to the total number of samples in each data set; Figure 4 inset). Samples compiled in pd15 and ag18 also show much broader bimodal or trimodal distributions across P's compared to a narrow unimodal P distribution centered at 1 GPa for recovered markers.

With respect to T, thermal gradients of recovered markers are significantly lower than natural samples. On average, markers recovered from <2 GPa differ from rocks exhumed from <2 GPa by 173°C and 3–4°C/km (excluding the highest-T samples in ag18 that relate to subduction initiation, Agard et al., 2018, 2020; Soret et al., 2022). Even within typical uncertainties for thermobarometry and phase equilibrium modeling (c. ±0.1–0.15 GPa and ±50°C, Kohn & Spear, 1991; Penniston-Dorland et al., 2015; Spear, 1993), major discrepancies exist between the high-frequency peak of recovered markers centered at 1 GPa and 275°C and the high-frequency peaks of natural samples centered at 1 GPa and 380°C and 2 GPa and 550°C (compare Figures 1 and 4). However, when comparing the distribution of samples around 1 GPa, rather than modal peak positions, moderate overlap does exist between T's of markers and natural samples.

### 3.1.2. Markers From Individual Numerical Experiments

For most experiments, marker recovery is localized within discrete and narrow multimodal distributions with step-like CDFs (e.g., 3). The PT positions of recovery clusters vary with subduction zone setting, however, so comparisons between individual numerical experiments and the rock record are challenging. For example, a few experiments show broad marker distributions that resemble the rock record with respect to P, but not with respect to thermal gradients (Supporting Information S1). Other experiments show the opposite. To better compare marker recovery among various subduction zone settings, we combined recovered markers from multiple numerical experiments with similar thermo-kinematic boundary conditions—analogous to randomly sampling exhumed HP rocks from similar subduction zones (Figures 5 and 6).

**Figure 4.** Pressure-temperature (PT) diagram showing the PT conditions of recovered markers (black point cloud) from all 64 numerical experiments and the frequency of recovered markers (green Tanaka contours) in comparison with the pd15 (solid red contours) and ag18 (filled gray contours) datasets. Marker frequency is concentrated along relatively cool thermal gradients, primarily near the continental Moho (1 GPa), with minor recovery modes centered near the onset of plate coupling (2.3–2.5 GPa). Thin lines are thermal gradients labeled in °C/km. Reaction boundaries for eclogitization of oceanic crust and antigorite dehydration are from Ito and Kennedy (1971) and Schmidt and Poli (1998), respectively. Marker counts (Tanaka contours) are computed across a 100 × 100 grid (0.04 GPa × 10°C). (insets) Probability distribution functions (top insets) and cumulative distribution functions (bottom inset) comparing P and T distributions between numerical experiments (green lines) and natural samples (pink lines: pd15, black lines: ag18). Note the higher-abundance of pd15 and ag18 samples at $P > 1.5$ GPa compared to markers.

Whether comparing the rock record with recovered markers from individual numerical experiments, suites of experiments, or all numerical experiments, several key observations emerge:

1. Recovered markers from most individual numerical experiments show discrete multimodal PT distributions with steep step-like CDFs (Figure 3 and Supporting Information S1)
2. While relatively few markers are recovered from PT regions coinciding with high-frequencies of natural samples around 2 GPa and 550°C, markers and natural samples recovered from near 1 GPa show moderate overlap (compare Figures 4–6)
3. Markers are frequently recovered from a major P mode near 1 GPa and very infrequently recovered between 2 and 2.5 GPa with a higher rate of recovery from lower P's (79% from ≤1.5 GPa) compared to natural samples (36%–59% from ≤1.5 GPa; compare Figures 4–6)
4. Markers are frequently recovered from a major T mode near 275°C and very infrequently recovered between 400 and 600°C with a higher rate of recovery from lower T's (97% from ≤525°C) compared to natural samples (44%–50% from ≤525°C; compare Figures 4–6)
5. The relative abundance of markers recovered along cooler thermal gradients for subduction zones (87% from 5 to 12°C/km) is high compared to natural samples (59%–78% from 5 to 12°C/km; compare Figures 4–6)
6. Many markers are recovered from the forbidden zone (11% from ≤5°C/km; compare Figures 4–6)
7. Virtually no markers (0.001%) are recovered from ≥15°C/km compared to natural samples (6%–30% from ≥15°C/km; compare Figures 4–6)

### 3.2. Comparing Markers Among Subduction Zone Settings

#### 3.2.1. Oceanic Plate Age Effect

Thermal gradients of recovered markers respond strongly to changes in oceanic plate age (Figure 7, Table A1). Both PT gradient modes are strongly inversely correlated with oceanic plate age, showing a mean increase from about $5.88 \pm 0.17$°C/km (Grad mode1) and $6.96 \pm 0.62$°C/km (Grad mode2) for older plates (≥85 Ma) to about $7.24 \pm 0.05$°C/km (Grad mode1) and $8.81 \pm 0.5$°C/km (Grad mode2) for younger plates (≤55 Ma). The dominant P mode (P mode1) moderately correlates with oceanic plate age, indicating a slightly higher possibility of recovering material from beyond the continental Moho for the oldest oceanic plates (≥85 Ma). Neither T modes, nor recovery rate correlate with oceanic plate age. Although oceanic plate age strongly affects the average PT gradients of recovered material, it does not strongly shift marker recovery up or down the subduction interface (e.g., compare average thermal gradients of markers between Figures 5 and 6).

#### 3.2.2. Convergence Velocity Effect

P's and T's of recovered markers respond strongly to changes in convergence velocity (Figure 7, Table A1). Both P modes are strongly inversely correlated with convergence velocity, showing a mean increase from $1.08 \pm 0.03$ GPa (P mode1) and $1.89 \pm 0.23$ GPa (P mode2) for fast moving plates (100 km/Ma) to about $1.39 \pm 0.1$ GPa (P mode1) and $2.63 \pm 0.16$ GPa (P mode2) for slow moving plates (40 km/Ma). However, the dominant P mode (P mode1) does not change significantly until convergence velocity drops below 66 km/Ma (Table A1). Both T modes are strongly inversely correlated with convergence velocity, showing a mean increase from $249 \pm 5.6$°C (T mode1) and $367.4 \pm 50.6$°C (T mode2) for fast moving plates (100 km/Ma) to about $311.7 \pm 1.5$°C (T mode1) and $541.7 \pm 79.8$°C (T mode2) for slow moving plates (40 km/Ma). Neither PT gradient modes, nor recovery rate correlate with convergence velocity. In summary, decreasing convergence velocity shifts marker recovery to
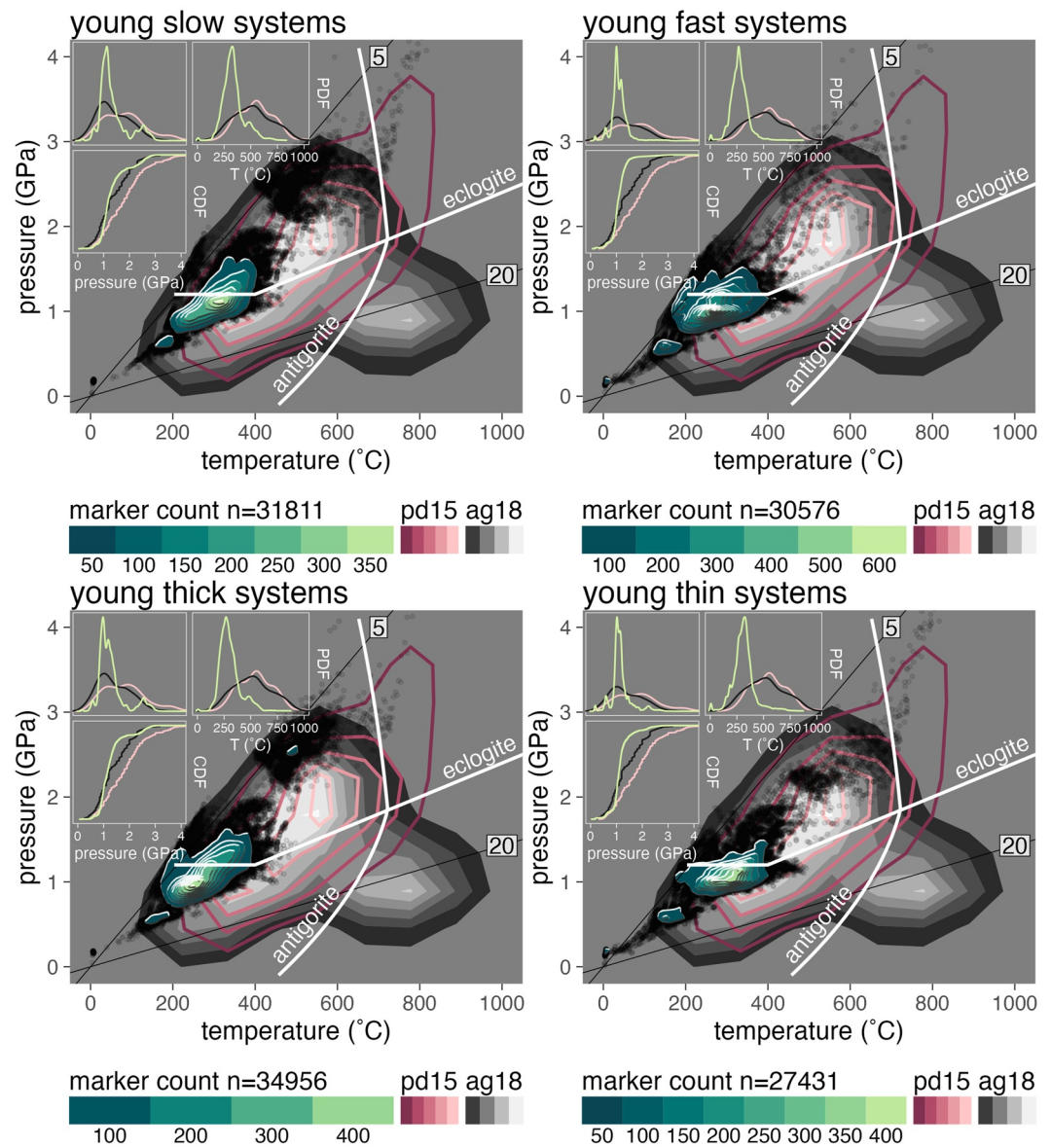
**Figure 5.** Pressure-temperature (PT) diagram showing the PT conditions of recovered markers (black point clouds) from numerical experiments with young oceanic plates (32.6–55 Ma) and the frequencies of recovered markers (green Tanaka contours) in comparison with the pd15 (solid red contours) and ag18 (filled gray contours) datasets, grouped by subduction zone setting (16 experiments per plot; boundary conditions summarized in Kerswell et al. (2021)). Thin lines are thermal gradients labeled in °C/km. Reaction boundaries for eclogitization of oceanic crust and antigorite dehydration are from Ito and Kennedy (1971) and Schmidt and Poli (1998), respectively. Marker counts (Tanaka contours) are computed across a $100 \times 100$ grid ($0.04$ GPa $\times 10$°C). (insets) Probability distribution functions (top insets) and cumulative distribution functions (bottom inset) comparing P and T distributions between numerical experiments (green lines) and natural samples (pink lines: pd15, black lines: ag18).

warmer and deeper conditions along the subduction interface without significantly changing the average thermal gradient of subducted material.

### 3.2.3. Upper-Plate Thickness Effect

A strong positive association between upper-plate thickness and mechanical coupling depths was demonstrated for the same numerical experiments used to trace markers (Kerswell et al., 2021). P distributions of markers were thus expected to respond strongly to changes in upper-plate thickness. However, a surprisingly negligible effect was observed (Figure 7). For example, neither of the P modes, nor T mode2 or Grad mode2 (usually the most
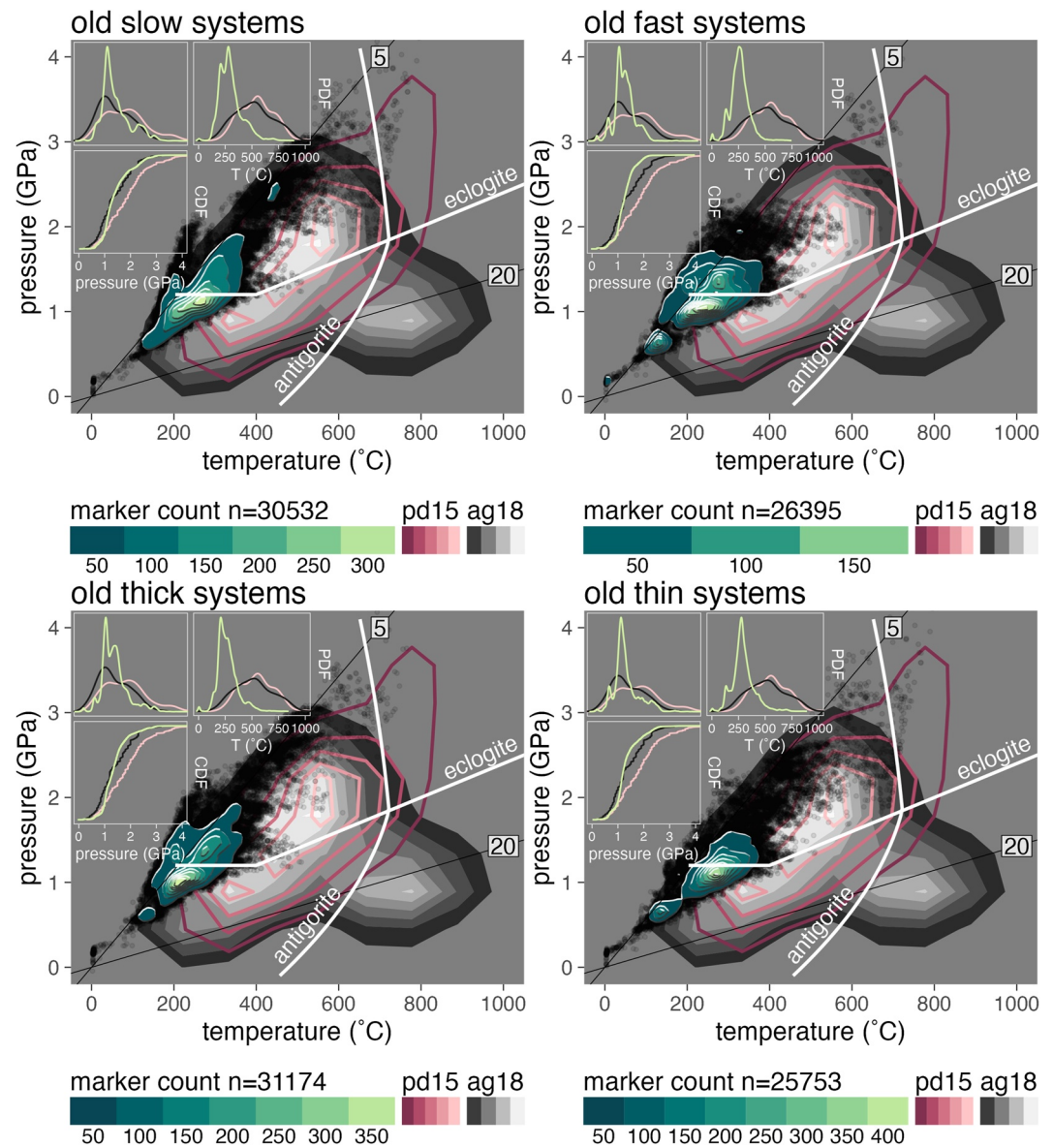
**Figure 6.** Pressure-temperature (PT) diagram showing the PT conditions of recovered markers (black point clouds) from numerical experiments with older oceanic plates (85–110 Ma) and the frequencies of recovered markers (green Tanaka contours) in comparison with the pd15 (solid red contours) and ag18 (filled gray contours) datasets, grouped by subduction zone setting (16 experiments per plot; boundary conditions summarized in Kerswell et al. (2021)). Thin lines are thermal gradients labeled in °C/km. Reaction boundaries for eclogitization of oceanic crust and antigorite dehydration are from Ito and Kennedy (1971) and Schmidt and Poli (1998), respectively. Marker counts (Tanaka contours) are computed across a $100 \times 100$ grid ($0.04$ GPa $\times$ $10°C$). (insets) Probability distribution functions (top insets) and cumulative distribution functions (bottom inset) comparing P and T distributions between numerical experiments (green lines) and natural samples (pink lines: pd15, black lines: ag18).

deeply subducted markers) correlate with upper-plate thickness. In contrast, the dominant PT gradient mode (Grad mode1) and T mode (T mode1) inversely correlate with upper-plate thickness. Recovery rate (ratio of recovered:subducted markers) is correlated with upper-plate thickness and not with any other boundary condition, indicating higher recovery rates are more likely underneath thick upper-plates. Recovery rates show a mean decrease from $10.65 \pm 0.28\%$ for thicker plates ($\geq 78$ km-thick) to $8.09 \pm 0.32\%$ for thinner upper-plates ($\leq 62$ km-thick). In summary, thin upper-plates are more likely to produce warmer thermal gradients, higher T's, and lower recovery rates.

## distributions of PT modes and recovery rates



## monotonic correlation test (always increasing or decreasing)
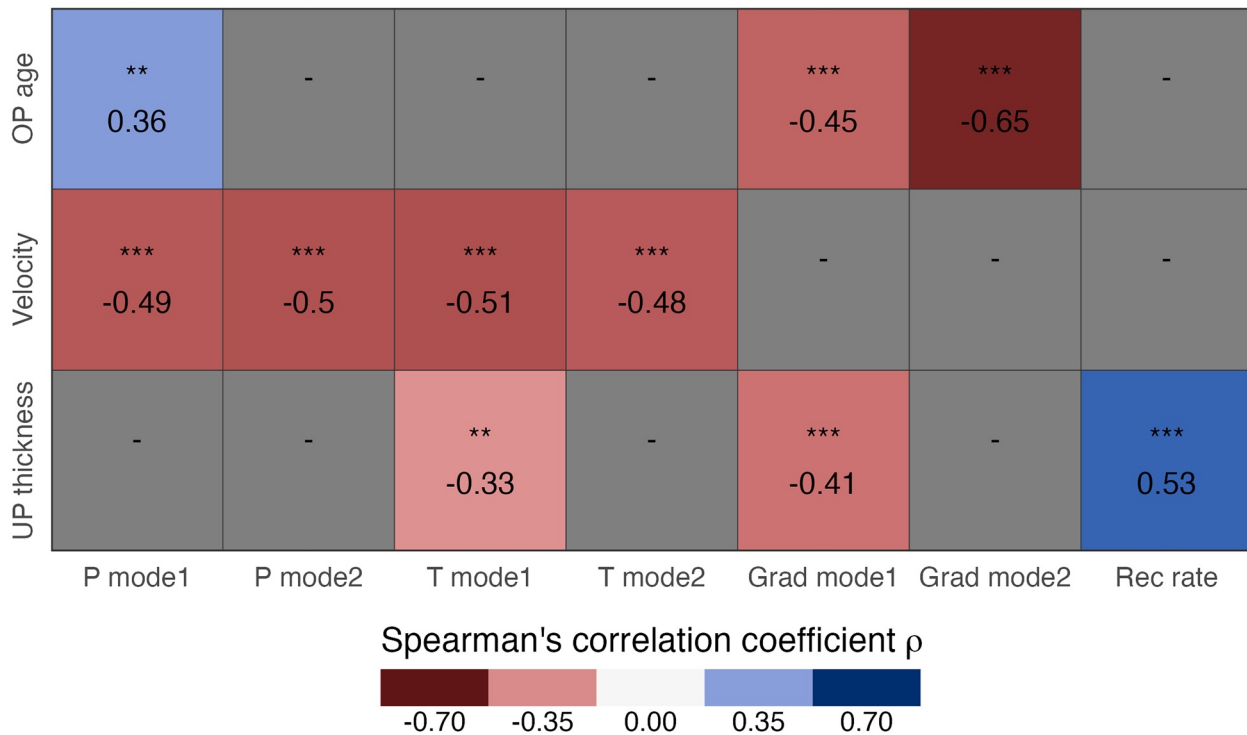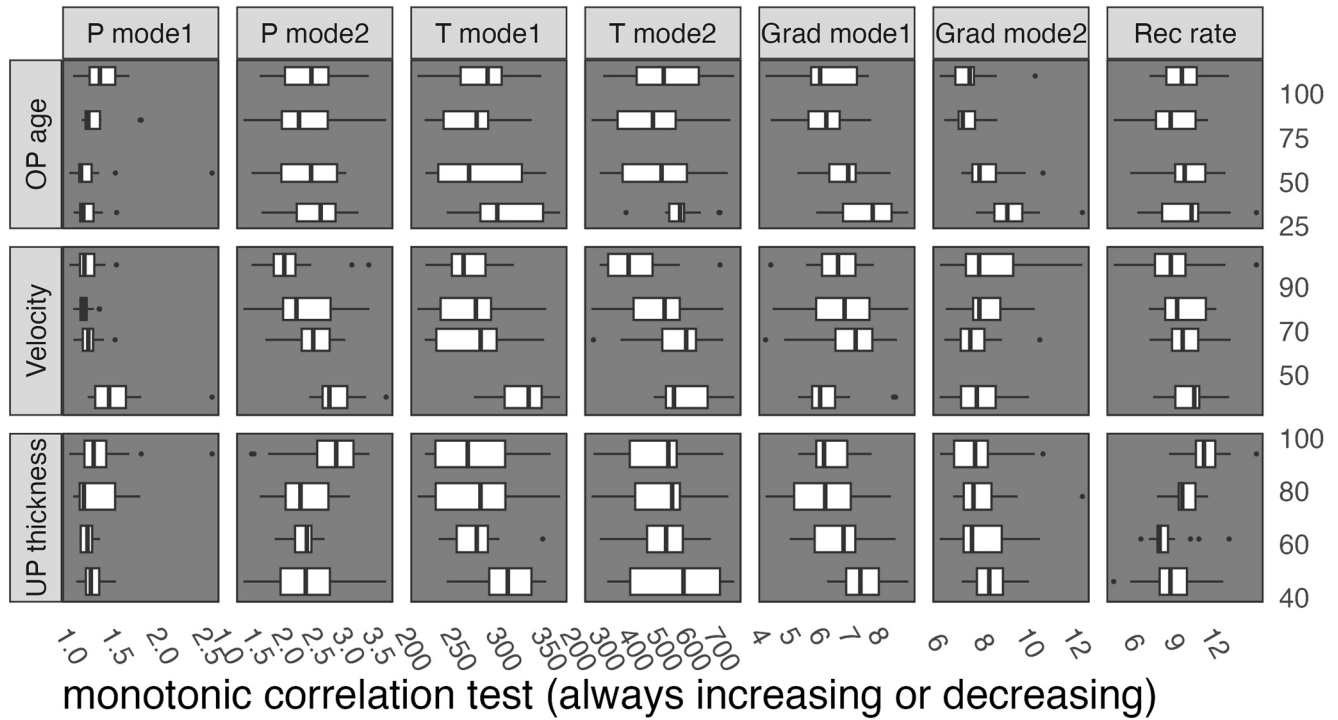


Figure 7.

## 4. Discussion

### 4.1. Thermo-Kinematic Controls on Rock Recovery

While the combined distribution of markers recovered from all numerical experiments shows appreciable deviations from PT estimates compiled by Penniston-Dorland et al. (2015) and Agard et al. (2018), markers recovered from simulations with the youngest oceanic plates (32.6–55 Ma) and the slowest convergence velocities (40–66 km/Ma) begin to resemble the distribution of exhumed HP rocks with respect to thermal gradients and P distributions (compare Figure 4 with Figures 5 and 6). Slower subduction of younger plates increases marker thermal gradients and strongly shifts marker recovery down the subduction interface (strong correlations with Grad and P modes, Figure 7). For example, experiments with the slowest convergence velocities have P CDF's that resemble ag18. It is important to note that old systems (with thin and thick upper-plates) also resemble ag18 with respect to their P CDF's, while on the other hand, all experiments deviate strongly from pd15 with respect to their P CDF's and show considerable thermal discrepancies with both pd15 and ag18 (especially lacking recovered markers above 525°C), regardless of thermo-kinematic boundary conditions (Figures 5 and 6).

The correlations in Figure 7 suggest a shift toward warmer recovery conditions could be complemented by thin upper-plates—implying systems with thin upper-plates, slow convergence, and young oceanic plates should be the most consistent with the distribution of rock recovery implied by pd15 and ag18 (Figure 5). This correspondence might appear consistent with arguments that the rock record is composed primarily of rock bodies exhumed from "warm" subduction settings (i.e., geodynamic bias, Abers et al., 2017; van Keken et al., 2018). However, our numerical experiments also show that recovery rates do not correlate with oceanic plate age or convergence velocity, and that recovery rates are poorer for thinner upper-plates (Figure 7). Poor correlations among recovery rates and important subduction zone parameters (except for upper-plate thickness) suggest that rock recovery, in terms of volumes of recovered material, is not largely dependent on subduction zone setting. The many tens of thousands of markers recovered from a wide variety of numerical experiments summarized in Figure 7 counter the notion that greater volumes of rock are preferentially recovered from "warm" subduction zone settings. However, since our analysis focused on recovery, rather than exhumation, we cannot rule out the possibility of preferential exhumation from certain PT conditions that might be implicitly represented in ag18 and pd15.

Besides recovery rates of subducting markers, other dynamic characteristics appear to correlate with oceanic plate age and convergence velocity. For example, simulations with slow convergence velocities (e.g., models: cda, cde, cdi, cdm) tend to have higher subduction angles (see Supporting Information S1) with thicker subduction interfaces that allow more markers to subduct to deeper, and thus warmer, conditions compared to other experiments (e.g., models: cdd, cdh, cdl, cdp) that form narrow interfaces with shallow choke points (e.g., see Supporting Information S1). Observationally, the angle of subduction does not correlate significantly with oceanic plate age or convergence velocity, but rather inversely with the duration of subduction (Hu & Gurnis, 2020). Thus, the rock record might indicate preferential exhumation during the earlier stages of subduction when subduction angles were steeper (although not necessarily during subduction initiation), even for older oceanic plates. More generally, differences in plate flexibility, overall subduction geometry, and velocity of plate motions strongly affect PT distributions of rock recovery (Monié & Agard, 2009)—rather than strictly "warm" versus "cool" subduction settings per se. In other words, thermo-kinematic boundary conditions typically inferred to strictly regulate *thermal* effects (e.g., young-slow oceanic plates supporting warmer thermal gradients) may indeed be regulating more *dynamic* effects (e.g., young-slow oceanic plates flexibly rolling back to support deeper subduction of material along thicker interfaces) that are subsequently *observed* as thermal effects (average increase in marker PT's).

**Figure 7.** (top) Distributions of marker recovery modes and recovery rates for all numerical experiments (Table A1). (bottom) Correlations among marker recovery modes and subduction zone settings. The dominant recovery mode (mode1) indicates the position of the tallest frequency peak with respect to P, T, or thermal gradient (i.e., conditions from which the greatest number of markers are recovered), while mode2 indicates the position of the warmest, deepest, or highest pressure-temperature gradient frequency peak (i.e., conditions from which very few deeply subducted markers are recovered; typically ≤1%–10% the number of markers in mode1). While oceanic plate age and upper-plate thickness more strongly affect the average thermal gradients of recovered markers (stronger correlations with gradient modes), convergence velocity more strongly affects the depths of recovery along the subduction interface, especially for deeply subducted markers (stronger correlations with P and T modes). Recovery rate correlates with upper-plate thickness, but not with any other boundary condition. Symbols indicate the Spearman's rank correlation coefficient that measures the significance of monotonic correlations. ***$\rho \leq 0.001$ (99.9% confidence), **$\rho \leq 0.01$ (99% confidence), *$\rho \leq 0.05$ (95% confidence), and - $\rho \geq 0.05$ (<95% confidence).

## 4.2. Comparison With Other Numerical Experiments

Marker PT distributions and their correlations with thermo-kinematic boundary conditions presented above are determined directly from large samples of recovered material evolving dynamically in a deforming subduction interface (analogous to reconstructing thermal gradients from large random samples of exhumed HP rocks). In contrast, other studies investigating thermal responses to variable boundary conditions typically determine PT gradients statically along discrete surfaces representing megathrust faults (e.g., Abers et al., 2006; Currie et al., 2004; Davies, 1999; Furukawa, 1993; Gao & Wang, 2014; McKenzie, 1969; Molnar & England, 1990; Peacock & Wang, 1999; Syracuse et al., 2010; van Keken et al., 2011, 2019; Wada & Wang, 2009) or dynamically by "finding" the subduction interface heuristically at each timestep (e.g., Arcay, 2017; Holt & Condit, 2021; Ruh et al., 2015). Other studies using similar geodynamic codes have traced many fewer markers (typically dozens vs. ~120,000; Faccenda et al., 2008; Gerya et al., 2002; Sizova et al., 2010; Yamato et al., 2007, 2008) from a narrower range of subduction zone settings, so they have less statistical rigor. This study stresses the importance of large sample sizes because individual marker PT paths can vary considerably within a single simulation. Important modes of recovery become apparent from high-frequency peaks only as more markers are traced. Furthermore, most other studies make no attempt to determine peak PT conditions related to detachment (but with some important exceptions, e.g., Roda et al., 2012, 2020), so marker PT paths are less analogous to PT paths determined by applying petrologic modeling.

## 4.3. Comparison With Geophysical Observations

The locations of important recovery modes determined from numerical experiments correspond closely with the depths of important mechanical transitions inferred from seismic imaging studies and surface heat flow observations. For example, the dominant recovery mode common among all numerical experiments at about 1 GPa (Table A1 and Figure 4) is consistent with a layer of low seismic velocities and high $V_p/V_s$ ratios observed at numerous subduction zones between 20 and 50 km depth (Bostock, 2013). While considerable unknowns persist about the nature of deformation in this region (Bostock, 2013; Tewksbury-Christle & Behr, 2021), the low-velocity zone, accompanied by low-frequency and slow-slip seismic events, is often interpreted as a transitional brittle-ductile shear zone that actively accommodates underplating of subducted material and/or formation of a tectonic mélange around the base of the continental Moho (Audet & Kim, 2016; Audet & Schaeffer, 2018; Bostock, 2013; Calvert et al., 2011, 2020; Delph et al., 2021).

Formation of low-velocity zones and their geophysical properties are generally attributed to high pore-fluid pressures caused by metamorphic reactions relating to the dehydration of oceanic crust (Hacker, 2008; Rondenay et al., 2008; van Keken et al., 2011). Surprisingly, despite our numerical implementation of a relatively simple model for dehydration of oceanic crust (Ito & Kennedy, 1971; Kerswell et al., 2021), and a relatively simple visco-plastic rheological model (Gerya & Yuen, 2003; Kerswell et al., 2021), the primary mode of marker recovery at $1.15 \pm 0.47$ GPa (2 $\sigma$, Table A1) coincides closely with the expected region for shallow underplating according to geophysical constraints ($35 \pm 15$ km or $1.0 \pm 0.4$ GPa). The size of the markers data set ($n = 119,314$ recovered markers) and prevalence of marker recovery from 1 GPa suggest that although dehydration may indeed trigger detachment of subducting rocks, other factors—notably the compositional and mechanical transition in the upper-plate across the Moho—also influence detachment at this depth.

The termination of the low-velocity zone at depths beyond the continental Moho marks another important mechanical transition. This second transition is often interpreted as the onset of mechanical plate coupling near 80 km (or 2.3 GPa, Agard et al., 2009, 2018; Furukawa, 1993; Monié & Agard, 2009; Plunder et al., 2015; Wada & Wang, 2009) and coincides well with the deeper recovery modes (P mode2) of markers at $2.2 \pm 1.1$ GPa (2 $\sigma$, Table A1). Although these deeper modes of marker recovery from near 2 GPa are noticeable in our numerical experiments and consistent with maximum recovery depths implied in pd15 and ag18, they represent a minor fraction of recovered markers—typically ≤1%–10% for individual numerical experiments. In other words, markers indicate maximum recovery depths that are consistent with the onset of plate coupling, but the relative frequency of material recovered from near 2 GPa in numerical experiments is inconsistent with the amount of material represented in pd15 and ag18 from the same conditions. Between the major mode of recovery at ~35–40 km and the few markers recovered from near ~80 km lies a gap in (or significant lack of) recovered markers that coincides with the highest sample frequencies of exhumed HP rocks compiled in pd15 and ag18 (Figure 4). This recovery gap is discussed in the following section.

### 4.4. The Marker Recovery Gap

Although recovered markers partially overlap with the range of PT estimates compiled in the pd15 and ag18 datasets, the differences between distributions of recovered markers and natural samples are numerous, including: (a) an obvious lack of markers recovered from ≥15°C/km (0.001%) compared to pd15 and ag18 (37%–48%, Figure 4), (b) recovery of markers from a single dominant mode near 1 GPa and 275°C compared to more broadly distributed multimodal recovery across PT space for natural samples (Figure 4), (c) a general shift toward lower T's and cooler thermal gradients for markers compared to natural samples, and (d) a remarkable gap in marker recovery near 2 GPa and 550°C that coincides with the highest frequency of natural samples (Figure 4). In fact, across 64 numerical experiments with wide-ranging initial conditions less than 1% (0.64%) of markers are recovered from between 1.8 and 2.2 GPa and 475–625°C. Why might this gap occur? Four possibilities are considered:

1. Simple rheological models preclude certain recovery mechanisms (poor implementation of subduction interface mechanics, i.e., modeling uncertainty, Section 4.4.1)
2. Peak metamorphic conditions are systematically misinterpreted (peak metamorphic conditions do not correspond to maxP or PT paths are not well constrained, i.e., petrologic uncertainties, Section 4.4.2, e.g., see Penniston-Dorland et al., 2015)
3. Rocks are frequently (re)sampled from the same peak metamorphic conditions and other rocks from different metamorphic grades are infrequently sampled (selective nonrandom sampling, i.e., scientific bias, Section 4.4.3, e.g., see Agard et al., 2018)
4. Rocks are recovered during short-lived events (e.g., subduction of seamounts, Agard et al., 2009) or by preferential exhumation mechanisms that are not implemented in our numerical experiments, rather than recovered during steady-state subduction within a serpentine-rich tectonic mélange that is characteristic of our numerical experiments (i.e., geodynamic uncertainties, Section 4.4.4)

### 4.4.1. Numerical Modeling Uncertainties

Simplifying assumptions in our numerical experiments influence thermal gradients and dynamics of rock recovery from the subducting oceanic plate. Substantially lower T's and thermal gradients in numerical experiments compared to natural samples (Figure 4) might indicate imperfect implementation of heat generation and transfer (Kohn et al., 2018; Penniston-Dorland et al., 2015). In the numerical experiments, our rheological model and implementation of serpentine formation in the upper mantle creates a weak interface. A stronger rheology (e.g., quartz or a mixed melange zone, Beall et al., 2019; Ioannidi et al., 2021), or a stronger serpentine flow law (Burdette & Hirth, 2022), would yield greater heating and higher T's from enhanced viscous dissipation (calculated as the product of deviatoric stress and strain rate in our experiments, Gerya, 2019) along the subduction interface (similar to increasing shear heating, e.g., Kohn et al., 2018). In principle, a stronger rheology might shift the overall PT distribution of markers to higher T's and help fill in the marker recovery gap around 2 GPa and 550°C, and/or possibly change flow to extract rocks more broadly along the subduction interface. Although the effects of different interface rheologies on thermal structure or rock recovery were not explicitly explored in this study, we note that numerical simulations with the smallest PT discrepancies between markers and natural samples (youngest oceanic plates and slowest convergence velocities, Figures 5 and 6) exhibit the same sizable gap in marker recovery around 2 GPa and 550°C. Thus, higher T's alone would not seem to close the gap.

Stronger interface rheologies would also change the distribution of strain within the interface shear zone and likely induce interface migration due to stronger coupling mechanics (e.g., Agard et al., 2020). Recovery rates and the P (depth) distributions of recovered rocks are therefore expected to be affected by interface strength, in addition to temperature. However, the geodynamics of coupling and interface migration are more complex than thermal effects. For example, it is possible to analytically predict the temperature increase due to viscous dissipation by evaluating the stress and strain rate terms in empirical flow laws for various viscosities (material strengths). On the other hand, it is not possible to analytically predict changes to interface morphology, position, or strain distribution as a function of rheological parameters. Numerical experiments are necessary to evaluate such complex geodynamic phenomena, so we propose a more systematic study of the effects of various interface rheologies on rock recovery as a topic for future research.

### 4.4.2. Petrologic Uncertainties

Interpreting peak metamorphic conditions of complex polymetamorphic rocks is challenging with many sources of uncertainties. However, a global shift in PT estimates of natural samples toward warmer conditions

compared to recovered markers would imply that decades of field observations, conventional thermobarometry (e.g., Spear & Selverstone, 1983), phase equilibria modeling (e.g., Connolly, 2005), trace element thermometry (e.g., Ferry & Watson, 2007; Kohn, 2020), and Raman Spectroscopy of Carbonaceous Material thermometry (Beyssac et al., 2002) from many independent localities worldwide (e.g., Agard et al., 2009, 2018; Angiboust et al., 2009, 2016; Angiboust, Langdon, et al., 2012; Avigad & Garfunkel, 1991; Monié & Agard, 2009; Plunder et al., 2013, 2015) have systematically misinterpreted the prograde and retrograde histories of exhumed HP rocks. The consistency of independent analytical techniques suggests systematic bias is unlikely and estimated uncertainties are generally too small for this argument to be viable (Penniston-Dorland et al., 2015).

### 4.4.3. Selective Sampling and Scientific Bias

At least two factors might lead to scientific bias. First, the application of conventional thermobarometry is easier for certain rock types and mineral assemblages (e.g., eclogite-facies metabasites and metapelitic schists) than for others (e.g., quartzites, metagraywackes). Second, certain subduction complexes expose more rocks than others. These factors lead to sampling bias, both in the rocks that are selected for analysis and which subduction complexes contribute most to compilations. For example, a PT condition of ∼2 GPa and 550°C typically yields assemblages that are both recognizable in the field (eclogites, *sensu stricto*, and kyanite- or chloritoid-schists) and amenable to thermobarometric calculations and petrologic modeling. This fact may lead to oversampling of the rocks that yield these PT conditions and the subduction zones that expose these rocks. In Penniston-Dorland et al. (2015), the western and central European Alps, which contain many rocks that equilibrated near this PT condition, represented ∼90 samples across <1,000 km (∼1 sample per 10 km), whereas the Himalaya and Andes, which contained more diverse PT conditions, represented only ∼1 sample per 300–400 km. Some subduction zones are not represented at all in these datasets (e.g., central and western Aleutians, Kamchatka, Izu-Bonin-Marianas, Philippines, Indonesia, Tonga-Kermadec, etc.), either because metamorphic rocks are not exposed (that we know of) or rock types are not amenable to petrologic investigation. Correcting for this type of bias is challenging because it would require large random samples of exhumed HP rocks from localities worldwide and development of new techniques for quantifying PT conditions in diverse rock types.

### 4.4.4. Short-Lived Events and Geodynamic Uncertainties

Detachment of rocks from the subducting slab might not occur randomly, but rather in response to specific events, such as subduction of asperities or seamounts (e.g., Agard et al., 2009) or abrupt fluid events. Yet no numerical models have attempted to model these events. In the case of seamounts, high surface roughness correlates with higher coefficients of friction (Gao & Wang, 2014). Higher friction increases heating and T's, driving subduction interface thermal gradients into the field of PT conditions defined by the pd15 and ag18 datasets (Kohn et al., 2018). If asperities become mechanically unstable at depths of ∼50–70 km, preferential detachment would create an "overabundance" of recorded PT conditions at moderate T (∼550°C) at ∼2 GPa, as observed.

Alternatively, although fluid release is modeled in our numerical experiments as continuous, it may occur sporadically in nature (Audet et al., 2009; Faccenda, 2014). Two dehydration reactions along the subduction interface that are particularly relevant, but not explicitly modeled in the numerical experiments are: the transformation of lawsonite to epidote, and the transformation of chlorite (plus quartz) to garnet (e.g., Angiboust & Agard, 2010; Baxter & Caddick, 2013; Vitale Brovarone & Agard, 2013). Although dehydration of lawsonite is nearly discontinuous in PT space, few rocks show clear evidence for lawsonite immediately prior to peak metamorphism (although such evidence can be subtle). In the context of equilibrium thermodynamics, chlorite dehydration should occur continuously below depths of ∼35 km (Baxter & Caddick, 2013; Schmidt & Poli, 1998, 2013), consistent with assumptions of many numerical geodynamic models. However, some research suggests substantial overstepping of this reaction, resulting in the abrupt formation of abundant garnet and release of water (Castro & Spear, 2017). Direct geochronology of garnet growth rates in subduction complexes also suggests rapid growth and water release (Dragovic et al., 2015). Because fluids are thought to help trigger brittle failure (earthquakes) that could detach rocks from the subducting slab surface, abrupt water release at a depth of ∼50–70 km might again result in an "overabundance" of recorded PT conditions at P's of ∼2 GPa. However, this explanation for abundant recovery of material from near 2 GPa would not directly explain higher T's, and would require relatively consistent degrees of overstepping in rocks of similar bulk composition, despite differences in subduction parameters (such as subduction rate) that must control rates of P- and T-increase. Similar to the proposed investigations regarding various interface rheologies (Section 4.4.1), a more systematic study of the effects of various

dehydration reactions on rock recovery is possible with numerical geodynamic models and should be a topic for future research.

## 5. Conclusions

This study traces PT paths of more than one million markers from 64 subduction simulations representing a large range of presently active subduction zones worldwide. Marker recovery is identified by implementing a "soft" clustering algorithm, and PT distributions of recovered markers are compared among models and with the rock record. Such a large data set presents a statistically robust portrait of important recovery modes (conditions under which most markers are detached) along the subduction interface. The three most important findings are as follows:

1. Numerical simulations with relatively simple (de)hydration models and visco-plastic interface rheologies simulate important recovery mechanisms near the base of the continental Moho around 1 GPa and 275°C (underplating and/or formation of tectonic mélanges) and near the depth of mechanical plate coupling around 2.3–2.5 GPa and 525°C. The pd15 and ag18 datasets also indicate preferential recovery near ∼1 GPa, although the frequency of samples is much lower than model predictions.
2. Subduction systems with young oceanic plates, slow convergence velocities, and thin upper-plate lithospheres are most consistent with the rock record, but it is unclear to what extent kinematic effects (young flexible oceanic plates with high subduction angles accommodating deeper subduction of material) rather than thermal effects (young oceanic plates supporting higher thermal gradients) drive changes in marker PT distributions. Comparing PT distributions of recovered markers from young-slow-thin numerical experiments with the rock record is not straightforward, however, because numerical experiments also indicate that recovery rates do not correlate with oceanic plate age or convergence velocity, and fewer markers are recovered from subduction systems with thin upper-plates.
3. While maximum marker recovery depths near 2.3–2.5 GPa in many numerical experiments is consistent with the onset of plate coupling and sudden decrease in sample frequency above 2.3–2.5 GPa in the rock record, very few markers are recovered from >1 GPa. A gap in (or significant lack of) marker recovery near 2 GPa and 550°C contrasts with the high frequencies of natural samples at this approximate PT condition. Explanations for this "overabundance" of natural samples might include selective sampling of rocks amenable to petrologic investigation (sampling bias), reaction overstepping (abrupt release of water triggering detachment of rock near 2 GPa and 550°C), or processes such as subduction of seamounts or exhumation mechanisms that are not included in numerical simulations. Future work targeting natural samples from a larger range of peak PT conditions and analyzing marker recovery from numerical geodynamic models that include new implementations of metamorphic (de)hydration reactions and interface rheologies might help resolve this discrepancy.

## Appendix A

### A1. Gaussian Mixture Models

Let the traced markers represent a $d$-dimensional array of $n$ random independent variables $x_i \in \mathbb{R}^{n \times d}$. Assume markers $x_i$ were drawn from $k$ discrete probability distributions with parameters $\Phi$. The probability distribution of markers $x_i$ can be modeled with a mixture of $k$ components (Equation A1):

$$p(x_i|\Phi) = \sum_{j=1}^{k} \pi_j p(x_i|\Theta_j) \tag{A1}$$

where $p(x_i|\Theta_j)$ is the probability of $x_i$ under the $j$th mixture component and $\pi_j$ is the mixture proportion representing the probability that $x_i$ belongs to the $j$th component $\left( \pi_j \geq 0; \sum_{j=1}^{k} \pi_j = 1 \right)$.

Assuming $\Theta_j$ describes a Gaussian probability distributions with mean $\mu_j$ and covariance $\Sigma_j$, Equation A1 becomes:

$$p(x_i|\Phi) = \sum_{j=1}^{k} \pi_j \mathcal{N}(x_i|\mu_j, \Sigma_j) \tag{A2}$$

where

$$\mathcal{N}(x_i | \mu_j, \Sigma_j) = \frac{\exp\left\{ -\frac{1}{2}(x_i - \mu_j)(x_i - \mu_j)^T \Sigma_j^{-1} \right\}}{\sqrt{\det(2\pi\Sigma_j)}} \tag{A3}$$

The parameters $\mu_j$ and $\Sigma_j$, representing the center and shape of each cluster, are estimated by maximizing the log of the likelihood function, $L(x_i | \Phi) = \prod_{i=1}^{n} p(x_i | \Phi)$:

$$\log \quad L(x_i | \Phi) = \log \prod_{i=1}^{n} p(x_i | \Phi) = \sum_{i=1}^{n} \log \left[ \sum_{j=1}^{k} \pi_j p(x_i | \Theta_j) \right] \tag{A4}$$

Taking the derivative of Equation A4 with respect to each parameter, $\pi$, $\mu$, $\Sigma$, setting the equation to zero, and solving for each parameter gives the maximum likelihood estimators:

$$
\begin{aligned}
N_j \quad &= \sum_{i=1}^{n} \omega_i \\
\pi_j \quad &= \frac{N_j}{n} \\
\mu_j \quad &= \frac{1}{N_j} \sum_{i=1}^{n} \omega_i x_i \\
\Sigma_j \quad &= \frac{1}{N_j} \sum_{i=1}^{n} \omega_i (x_i - \mu_j)(x_i - \mu_j)^T
\end{aligned}
\tag{A5}
$$

where $\omega_i \left( \omega_i \geq 0; \sum_{j=1}^{k} \omega_i = 1 \right)$ are membership weights representing the probability of an observation $x_i$ belonging to the $j$th Gaussian and $N_j$ represents the number of observations belonging to the $j$th Gaussian. Please note that $\omega_i$ is unknown for markers so the maximum likelihood estimator cannot be computed with Equation A5. The solution to this problem is the Expectation-Maximization algorithm, which is defined below.

General purpose functions in the R package `Mclust` (Scrucca et al., 2016) are used to fit Gaussian mixture models. "Fitting" refers to adjusting all $k$ Gaussian parameters $\mu_j$ and $\Sigma_j$ until the data and Gaussian ellipsoids achieve maximum likelihood defined by Equation A4. After Banfield and Raftery (1993), covariance matrices $\Sigma$ in `Mclust` are parameterized to be flexible in their shape, volume, and orientation (Scrucca et al., 2016):

$$\Sigma_j = \lambda_j D_j A_j D_j^T \tag{A6}$$

where $D_j$ is the orthogonal eigenvector matrix, $A_j$ and $\lambda_j$ are diagonal matrices of values proportional to the eigenvalues. This implementation allows fixing one, two, or three geometric elements of the covariance matrices. That is, the volume $\lambda_j$, shape $A_j$, and orientation $D_j$ of Gaussian clusters can change or be fixed among all $k$ clusters (e.g., Celeux & Govaert, 1995; Fraley & Raftery, 2002). Fourteen parameterizations of Equation A6 are tried, representing different geometric combinations of the covariance matrices $\Sigma$ (see Scrucca et al., 2016) and the Bayesian information criterion is computed (Schwarz, 1978). The parameterization for Equation A6 is chosen by Bayesian information criterion.

## A2. Expectation-Maximization

The Expectation-Maximization algorithm estimates Gaussian mixture model parameters by initializing $k$ Gaussians with parameters $(\pi_j, \mu_j, \Sigma_j)$, then iteratively computing membership weights with Equation A7 and updating Gaussian parameters with Equation A5 until reaching a convergence threshold (Dempster et al., 1977).

The *expectation* (E-)step involves a "latent" multinomial variable $z_i \in \{1, 2, \ldots, k\}$ representing the unknown classifications of $x_i$ with a joint distribution $p(x_i, z_i) = p(x_i | z_i)p(z_j)$. Membership weights $\omega_i$ are equivalent to the conditional probability $p(z_i | x_i)$, which represents the probability of observation $x_i$ belonging to the $j$th Gaussian. Given initial guesses for Gaussian parameters $\pi_j, \mu_j, \Sigma_j$, membership weights are computed using Bayes Theorem (E-step):

$$p(z_i | x_i) = \frac{p(x_i | z_i)p(z_j)}{p(x_i)} = \frac{\pi_j \mathcal{N}(\mu_j, \Sigma_j)}{\sum_{j=1}^{k} \pi_j \mathcal{N}(\mu_j, \Sigma_j)} = \omega_i \tag{A7}$$

and Gaussian estimates are updated during the *maximization* (M-)step by applying $\omega_i$ to Equation A5. This step gives markers $x_i$ class labels $z_i \in \{1, \ldots, k\}$ representing assignment to one of $k$ clusters (Figure 2).

### A3. Marker Classification Results

Below are the classification results for all 64 numerical experiments presented in the main text (Table A1).

**Table A1**
*Subduction Zone Parameters and Marker Classification Summary*

| | Initial boundary conditions | | | | | Marker classification summary | | | | | | |
|---|---|---|---|---|---|---|---|---|---|---|---|---|
| Model | $\Phi$ (km) | $Z_{UP}$ (km) | Age (Ma) | $\vec{v}$ (km/ Ma) | Recovered | Rec. rate (%) | P mode1 (GPa) | P mode2 (GPa) | T mode1 (°C) | T mode2 (°C) | Grad mode1 (°C/km) | Grad mode2 (°C/km) |
| cda46 | 13.0 | 46 | 32.6 | 40 | 1,482 ± 26 | 7.8 ± 0.14 | 1.12 ± 0.00 | 2.43 ± 0.20 | 336 ± 2 | 595 ± 172 | 8.2 ± 0.02 | 9.5 ± 0.08 |
| cda62 | 13.0 | 62 | 32.6 | 40 | 1,352 ± 30 | 7.2 ± 0.16 | 1.12 ± 0.00 | 2.2 ± 0.16 | 333 ± 2 | 529 ± 4 | 8.3 ± 0.02 | 8.3 ± 0.02 |
| cda78 | 13.0 | 78 | 32.6 | 40 | 1,861 ± 26 | 9.8 ± 0.14 | 1.39 ± 0.00 | 2.38 ± 0.00 | 352 ± 2 | 477 ± 2 | 5.9 ± 0.02 | 9.1 ± 2.02 |
| cda94 | 13.0 | 94 | 32.6 | 40 | 1,933 ± 30 | 10.2 ± 0.16 | 1.24 ± 0.00 | 2.64 ± 0.00 | 341 ± 0 | 499 ± 2 | 5.6 ± 0.00 | 7.8 ± 0.04 |
| cdb46 | 21.5 | 46 | 32.6 | 66 | 1,809 ± 34 | 9.6 ± 0.18 | 1.04 ± 0.00 | 2.39 ± 0.62 | 334 ± 2 | 658 ± 4 | 8.3 ± 0.06 | 8.4 ± 0.46 |
| cdb62 | 21.5 | 62 | 32.6 | 66 | 1,406 ± 28 | 7.4 ± 0.16 | 1 ± 0.00 | 2.16 ± 0.00 | 281 ± 2 | 534 ± 30 | 7.8 ± 0.04 | 10 ± 0.06 |
| cdb78 | 21.5 | 78 | 32.6 | 66 | 1,889 ± 20 | 10 ± 0.12 | 0.92 ± 0.00 | 2.51 ± 0.14 | 264 ± 2 | 541 ± 10 | 8.1 ± 0.04 | 8.1 ± 0.04 |
| cdb94 | 21.5 | 94 | 32.6 | 66 | 2,353 ± 56 | 12.5 ± 0.30 | 1.14 ± 0.08 | 2.63 ± 0.02 | 291 ± 2 | 471 ± 82 | 7.5 ± 0.02 | 7.8 ± 1.00 |
| cdc46 | 26.1 | 46 | 32.6 | 80 | 1,721 ± 50 | 9.1 ± 0.26 | 1.02 ± 0.00 | 1.41 ± 0.92 | 320 ± 2 | 487 ± 154 | 8.7 ± 0.28 | 9.2 ± 1.10 |
| cdc62 | 26.1 | 62 | 32.6 | 80 | 1,288 ± 18 | 6.8 ± 0.10 | 0.99 ± 0.00 | 2.01 ± 0.00 | 264 ± 2 | 531 ± 4 | 6.7 ± 0.04 | 8.7 ± 0.26 |
| cdc78 | 26.1 | 78 | 32.6 | 80 | 1,806 ± 28 | 9.6 ± 0.14 | 0.93 ± 0.10 | 2.87 ± 0.18 | 284 ± 2 | 516 ± 20 | 7.8 ± 0.04 | 7.9 ± 1.18 |
| cdc94 | 26.1 | 94 | 32.6 | 80 | 2,153 ± 32 | 11.4 ± 0.18 | 1.14 ± 0.00 | 3.01 ± 0.02 | 274 ± 0 | 533 ± 2 | 6.7 ± 0.02 | 9.8 ± 0.04 |
| cdd46 | 32.6 | 46 | 32.6 | 100 | 1,049 ± 62 | 5.6 ± 0.32 | 1 ± 0.00 | 1.77 ± 0.12 | 227 ± 2 | 470 ± 2 | 6 ± 0.02 | 8.6 ± 0.06 |
| cdd62 | 32.6 | 62 | 32.6 | 100 | 1,366 ± 20 | 7.2 ± 0.10 | 0.99 ± 0.00 | 1.63 ± 0.18 | 263 ± 2 | 334 ± 44 | 5.6 ± 0.08 | 8.9 ± 0.04 |
| cdd78 | 32.6 | 78 | 32.6 | 100 | 1,887 ± 32 | 10 ± 0.18 | 1 ± 0.00 | 1.94 ± 0.00 | 264 ± 0 | 513 ± 8 | 7.5 ± 0.04 | 11.8 ± 1.58 |
| cdd94 | 32.6 | 94 | 32.6 | 100 | 2,712 ± 32 | 14.4 ± 0.18 | 1.23 ± 0.00 | 2.9 ± 0.00 | 237 ± 26 | 661 ± 4 | 7.3 ± 0.02 | 7.3 ± 0.02 |
| cde46 | 22.0 | 46 | 55.0 | 40 | 1,613 ± 42 | 8.5 ± 0.22 | 1.11 ± 0.00 | 2.81 ± 0.44 | 315 ± 2 | 688 ± 102 | 6.7 ± 0.02 | 8.1 ± 1.10 |
| cde62 | 22.0 | 62 | 55.0 | 40 | 1,793 ± 42 | 9.5 ± 0.22 | 1.08 ± 0.00 | 2.24 ± 0.00 | 285 ± 2 | 485 ± 2 | 6.1 ± 0.02 | 7.4 ± 0.74 |
| cde78 | 22.0 | 78 | 55.0 | 40 | 1,868 ± 26 | 9.9 ± 0.14 | 1.38 ± 0.16 | 2.52 ± 0.00 | 315 ± 2 | 523 ± 170 | 5.8 ± 0.06 | 7.4 ± 0.04 |
| cde94 | 22.0 | 94 | 55.0 | 40 | 1,804 ± 22 | 9.5 ± 0.12 | 2.44 ± 0.64 | 2.54 ± 0.00 | 319 ± 2 | 430 ± 2 | 5 ± 0.02 | 7.2 ± 0.04 |
| cdf46 | 36.3 | 46 | 55.0 | 66 | 2,246 ± 62 | 11.9 ± 0.34 | 1.11 ± 0.04 | 2.7 ± 0.32 | 308 ± 2 | 672 ± 20 | 7.6 ± 0.04 | 7.6 ± 0.04 |
| cdf62 | 36.3 | 62 | 55.0 | 66 | 1,577 ± 26 | 8.4 ± 0.14 | 1.14 ± 0.00 | 2.21 ± 0.02 | 264 ± 2 | 577 ± 92 | 6.9 ± 0.02 | 6.9 ± 0.02 |
| cdf78 | 36.3 | 78 | 55.0 | 66 | 1,623 ± 22 | 8.6 ± 0.12 | 0.99 ± 0.00 | 2.73 ± 0.24 | 227 ± 2 | 546 ± 8 | 7 ± 0.02 | 7.2 ± 0.98 |
| cdf94 | 36.3 | 94 | 55.0 | 66 | 1,962 ± 38 | 10.4 ± 0.20 | 0.93 ± 0.00 | 2.79 ± 0.00 | 216 ± 0 | 547 ± 204 | 6.6 ± 0.02 | 6.6 ± 0.02 |
| cdg46 | 44.0 | 46 | 55.0 | 80 | 2,107 ± 56 | 11.2 ± 0.30 | 1.2 ± 0.00 | 1.97 ± 0.04 | 337 ± 10 | 338 ± 2 | 8.1 ± 0.16 | 8.2 ± 1.04 |
| cdg62 | 44.0 | 62 | 55.0 | 80 | 1,345 ± 36 | 7.1 ± 0.18 | 1 ± 0.00 | 1.74 ± 0.06 | 218 ± 4 | 272 ± 28 | 5.2 ± 0.02 | 7.5 ± 0.02 |
| cdg78 | 44.0 | 78 | 55.0 | 80 | 1,578 ± 36 | 8.4 ± 0.20 | 1.01 ± 0.00 | 2.17 ± 0.30 | 238 ± 2 | 518 ± 174 | 4.9 ± 0.02 | 7.1 ± 0.02 |
| cdg94 | 44.0 | 94 | 55.0 | 80 | 2,133 ± 24 | 11.3 ± 0.12 | 0.98 ± 0.00 | 2.65 ± 0.54 | 209 ± 2 | 407 ± 20 | 6.4 ± 0.02 | 9.4 ± 0.10 |
| cdh46 | 55.0 | 46 | 55.0 | 100 | 950 ± 20 | 5 ± 0.10 | 0.95 ± 0.00 | 1.59 ± 0.00 | 274 ± 2 | 352 ± 4 | 7.1 ± 0.06 | 8.9 ± 1.50 |
| cdh62 | 55.0 | 62 | 55.0 | 100 | 1,445 ± 22 | 7.7 ± 0.12 | 0.99 ± 0.00 | 1.73 ± 0.00 | 237 ± 34 | 243 ± 2 | 6.9 ± 1.44 | 7.1 ± 0.02 |
| cdh78 | 55.0 | 78 | 55.0 | 100 | 1,629 ± 28 | 8.6 ± 0.14 | 0.99 ± 0.00 | 1.62 ± 0.20 | 214 ± 6 | 242 ± 54 | 6.7 ± 0.86 | 6.8 ± 0.06 |
| cdh94 | 55.0 | 94 | 55.0 | 100 | 2,281 ± 34 | 12.1 ± 0.18 | 0.88 ± 0.00 | 1.24 ± 0.12 | 203 ± 0 | 275 ± 2 | 6.7 ± 0.02 | 10.1 ± 0.54 |
| cdi46 | 34.0 | 46 | 85.0 | 40 | 1,271 ± 58 | 6.7 ± 0.32 | 1.17 ± 0.00 | 3.47 ± 0.76 | 287 ± 2 | 697 ± 184 | 6.6 ± 0.02 | 6.6 ± 0.02 |
| cdi62 | 34.0 | 62 | 85.0 | 40 | 1,910 ± 24 | 10.1 ± 0.12 | 1.21 ± 0.72 | 2.28 ± 0.00 | 257 ± 0 | 462 ± 198 | 5.5 ± 0.64 | 6.7 ± 0.06 |
| cdi78 | 34.0 | 78 | 85.0 | 40 | 2,038 ± 32 | 10.8 ± 0.16 | 1.65 ± 0.02 | 2.56 ± 0.00 | 320 ± 2 | 444 ± 2 | 5.4 ± 0.02 | 6.5 ± 0.02 |

**Table** *A1*
*Continued*

| | Initial boundary conditions | | | | Marker classification summary | | | | | | | |
|---|---|---|---|---|---|---|---|---|---|---|---|---|
| Model | $\Phi$ (km) | $Z_{UP}$ (km) | Age (Ma) | $\vec{v}$ (km/Ma) | Recovered | Rec. rate (%) | P mode1 (GPa) | P mode2 (GPa) | T mode1 (°C) | T mode2 (°C) | Grad mode1 (°C/km) | Grad mode2 (°C/km) |
| cdi94 | 34.0 | 94 | 85.0 | 40 | 2,008 ± 30 | 10.6 ± 0.16 | 1.66 ± 0.00 | 3.03 ± 0.94 | 292 ± 2 | 503 ± 118 | 5 ± 0.02 | 6.7 ± 1.36 |
| cdj46 | 56.1 | 46 | 85.0 | 66 | 1,640 ± 116 | 8.7 ± 0.62 | 1.07 ± 0.00 | 2.49 ± 0.66 | 272 ± 2 | 581 ± 352 | 6.5 ± 0.38 | 7.4 ± 0.10 |
| cdj62 | 56.1 | 62 | 85.0 | 66 | 1,360 ± 32 | 7.2 ± 0.16 | 1.09 ± 0.00 | 2.12 ± 0.08 | 238 ± 0 | 519 ± 22 | 6.3 ± 0.02 | 6.3 ± 0.02 |
| cdj78 | 56.1 | 78 | 85.0 | 66 | 1,324 ± 28 | 7 ± 0.16 | 1.22 ± 0.00 | 1.94 ± 0.10 | 202 ± 0 | 315 ± 2 | 4.5 ± 0.02 | 6.5 ± 0.18 |
| cdj94 | 56.1 | 94 | 85.0 | 66 | 1,846 ± 34 | 9.8 ± 0.18 | 1.03 ± 0.00 | 1.52 ± 0.02 | 205 ± 0 | 221 ± 166 | 5.9 ± 0.02 | 5.9 ± 0.02 |
| cdk46 | 68.0 | 46 | 85.0 | 80 | 1,465 ± 26 | 7.8 ± 0.14 | 1.06 ± 0.02 | 1.11 ± 0.26 | 271 ± 2 | 368 ± 154 | 7.4 ± 0.02 | 7.4 ± 0.02 |
| cdk62 | 68.0 | 62 | 85.0 | 80 | 1,208 ± 16 | 6.4 ± 0.08 | 1.07 ± 0.00 | 1.83 ± 0.00 | 220 ± 2 | 449 ± 170 | 4.7 ± 0.02 | 6.7 ± 0.04 |
| cdk78 | 68.0 | 78 | 85.0 | 80 | 1,537 ± 32 | 8.1 ± 0.16 | 1.01 ± 0.04 | 1.8 ± 0.32 | 214 ± 6 | 214 ± 6 | 6.1 ± 1.10 | 7.2 ± 1.54 |
| cdk94 | 68.0 | 94 | 85.0 | 80 | 2,030 ± 32 | 10.8 ± 0.18 | 1.04 ± 0.00 | 3.2 ± 0.04 | 263 ± 22 | 673 ± 24 | 6 ± 0.04 | 6 ± 0.04 |
| cdl46 | 85.0 | 46 | 85.0 | 100 | 718 ± 18 | 3.8 ± 0.10 | 1.1 ± 0.00 | 1.56 ± 0.02 | 268 ± 2 | 268 ± 2 | 6 ± 0.06 | 6.8 ± 3.26 |
| cdl62 | 85.0 | 62 | 85.0 | 100 | 1,099 ± 18 | 5.8 ± 0.10 | 1.02 ± 0.00 | 2.23 ± 0.02 | 246 ± 2 | 412 ± 62 | 6.7 ± 0.24 | 6.7 ± 0.24 |
| cdl78 | 85.0 | 78 | 85.0 | 100 | 1,667 ± 32 | 8.9 ± 0.16 | 1.06 ± 0.00 | 1.94 ± 0.02 | 273 ± 2 | 273 ± 2 | 4 ± 0.02 | 8.2 ± 3.30 |
| cdl94 | 85.0 | 94 | 85.0 | 100 | 1,489 ± 80 | 7.9 ± 0.42 | 1.23 ± 0.18 | 1.28 ± 0.12 | 224 ± 4 | 356 ± 106 | 5.8 ± 0.06 | 7.5 ± 2.60 |
| cdm46 | 44.0 | 46 | 110.0 | 40 | 1,392 ± 20 | 7.4 ± 0.10 | 1.39 ± 0.00 | 3.14 ± 0.02 | 320 ± 2 | 711 ± 6 | 6.1 ± 0.02 | 8.2 ± 1.88 |
| cdm62 | 44.0 | 62 | 110.0 | 40 | 2,332 ± 32 | 12.3 ± 0.16 | 1.21 ± 0.00 | 2.45 ± 0.00 | 281 ± 2 | 439 ± 2 | 5.5 ± 0.38 | 5.7 ± 0.18 |
| cdm78 | 44.0 | 78 | 110.0 | 40 | 1,830 ± 32 | 9.7 ± 0.18 | 1.48 ± 0.00 | 2.51 ± 0.00 | 331 ± 4 | 691 ± 188 | 5.5 ± 0.02 | 6.5 ± 1.26 |
| cdm94 | 44.0 | 94 | 110.0 | 40 | 1,899 ± 36 | 10.1 ± 0.18 | 1.53 ± 0.00 | 2.87 ± 0.00 | 302 ± 2 | 495 ± 128 | 5.3 ± 0.02 | 6 ± 0.02 |
| cdn46 | 72.6 | 46 | 110.0 | 66 | 1,930 ± 46 | 10.2 ± 0.24 | 1.25 ± 0.00 | 2.31 ± 0.06 | 283 ± 2 | 647 ± 34 | 7.1 ± 0.04 | 7.1 ± 0.04 |
| cdn62 | 72.6 | 62 | 110.0 | 66 | 1,218 ± 30 | 6.5 ± 0.16 | 1.13 ± 0.00 | 2.15 ± 0.24 | 269 ± 0 | 573 ± 2 | 6.9 ± 0.04 | 6.9 ± 0.04 |
| cdn78 | 72.6 | 78 | 110.0 | 66 | 1,681 ± 44 | 8.9 ± 0.24 | 1.38 ± 0.00 | 1.47 ± 0.40 | 213 ± 2 | 429 ± 4 | 3.9 ± 0.10 | 6.8 ± 0.14 |
| cdn94 | 72.6 | 94 | 110.0 | 66 | 1,681 ± 32 | 8.9 ± 0.16 | 1.06 ± 0.00 | 1.75 ± 0.36 | 202 ± 4 | 321 ± 140 | 5.6 ± 0.04 | 6.4 ± 0.80 |
| cdo46 | 88.0 | 46 | 110.0 | 80 | 1,477 ± 138 | 7.8 ± 0.74 | 1.21 ± 0.02 | 1.77 ± 0.88 | 280 ± 0 | 336 ± 80 | 7.4 ± 0.04 | 7.4 ± 0.04 |
| cdo62 | 88.0 | 62 | 110.0 | 80 | 1,342 ± 24 | 7.1 ± 0.12 | 1.06 ± 0.02 | 2.36 ± 0.52 | 253 ± 4 | 630 ± 42 | 7.1 ± 0.06 | 7.1 ± 0.06 |
| cdo78 | 88.0 | 78 | 110.0 | 80 | 1,627 ± 28 | 8.6 ± 0.16 | 0.92 ± 0.00 | 1.38 ± 0.02 | 194 ± 2 | 383 ± 74 | 4.1 ± 0.02 | 7.1 ± 1.36 |
| cdo94 | 88.0 | 94 | 110.0 | 80 | 1,989 ± 148 | 10.6 ± 0.80 | 1.06 ± 0.16 | 2.52 ± 1.92 | 255 ± 2 | 492 ± 422 | 5.7 ± 0.02 | 7.2 ± 2.50 |
| cdp46 | 110.0 | 46 | 110.0 | 100 | 1,541 ± 160 | 8.2 ± 0.84 | 1.27 ± 0.00 | 1.8 ± 1.92 | 301 ± 2 | 310 ± 38 | 7 ± 0.06 | 7 ± 0.06 |
| cdp62 | 110.0 | 62 | 110.0 | 100 | 1,361 ± 104 | 7.2 ± 0.56 | 1.12 ± 0.00 | 2.06 ± 0.00 | 234 ± 2 | 393 ± 322 | 5.2 ± 0.72 | 9.8 ± 1.44 |
| cdp78 | 110.0 | 78 | 110.0 | 100 | 1,647 ± 42 | 8.8 ± 0.22 | 1.11 ± 0.00 | 1.81 ± 0.26 | 274 ± 2 | 521 ± 86 | 6 ± 1.16 | 6.3 ± 0.04 |
| cdp94 | 110.0 | 94 | 110.0 | 100 | 1,873 ± 168 | 9.9 ± 0.88 | 1.39 ± 0.16 | 3.18 ± 0.66 | 245 ± 0 | 254 ± 74 | 5.7 ± 0.02 | 5.7 ± 0.02 |

*Note.* Classifier uncertainties ($2\sigma$) estimated by running the classifier 30 times with random marker samples (jackknife sample proportion: 90%).

## Data Availability Statement

# References

Abers, G., van Keken, P., & Hacker, B. (2017). The cold and relatively dry nature of mantle forearcs in subduction zones. *Nature Geoscience*, *10*(5), 333–337. https://doi.org/10.1038/ngeo2922

Abers, G., van Keken, P., Kneller, E., Ferris, A., & Stachnik, J. (2006). The thermal structure of subduction zones constrained by seismic imaging: Implications for slab dehydration and wedge flow. *Earth and Planetary Science Letters*, *241*(3–4), 387–397. https://doi.org/10.1016/j.epsl.2005.11.055

Abers, G., van Keken, P., & Wilson, C. (2020). Deep decoupling in subduction zones: Observations and temperature limits. *Geosphere*, *16*(6), 1408–1424. https://doi.org/10.1130/ges02278.1

Agard, P. (2021). Subduction of oceanic lithosphere in the Alps: Selective and archetypal from (slow-spreading) oceans. *Earth-Science Reviews*, *214*, 103517. https://doi.org/10.1016/j.earscirev.2021.103517

Agard, P., Plunder, A., Angiboust, S., Bonnet, G., & Ruh, J. (2018). The subduction plate interface: Rock record and mechanical coupling (from long to short time scales). *Lithos*, *320–321*, 537–566. https://doi.org/10.1016/j.lithos.2018.09.029

Agard, P., Prigent, C., Soret, M., Dubacq, B., Guillot, S., & Deldicque, D. (2020). Slabitization: Mechanisms controlling subduction development and viscous coupling. *Earth-Science Reviews*, *208*, 103259. https://doi.org/10.1016/j.earscirev.2020.103259

Agard, P., Yamato, P., Jolivet, L., & Burov, E. (2009). Exhumation of oceanic blueschists and eclogites in subduction zones: Timing and mechanisms. *Earth-Science Reviews*, *92*(1–2), 53–79. https://doi.org/10.1016/j.earscirev.2008.11.002

Agard, P., Yamato, P., Soret, M., Prigent, C., Guillot, S., Plunder, A., et al. (2016). Plate interface rheological switches during subduction infancy: Control on slab penetration and metamorphic sole formation. *Earth and Planetary Science Letters*, *451*, 208–220. https://doi.org/10.1016/j.epsl.2016.06.054

Angiboust, S., & Agard, P. (2010). Initial water budget: The key to detaching large volumes of eclogitized oceanic crust along the subduction channel? *Lithos*, *120*(3–4), 453–474. https://doi.org/10.1016/j.lithos.2010.09.007

Angiboust, S., Agard, P., Glodny, J., Omrani, J., & Oncken, O. (2016). Zagros blueschists: Episodic underplating and long-lived cooling of a subduction zone. *Earth and Planetary Science Letters*, *443*, 48–58. https://doi.org/10.1016/j.epsl.2016.03.017

Angiboust, S., Agard, P., Jolivet, L., & Beyssac, O. (2009). The Zermatt-Saas ophiolite: The largest (60-km wide) and deepest (c. 70–80 km) continuous slice of oceanic lithosphere detached from a subduction zone? *Terra Nova*, *21*(3), 171–180. https://doi.org/10.1111/j.1365-3121.2009.00870.x

Angiboust, S., Agard, P., Raimbourg, H., Yamato, P., & Huet, B. (2011). Subduction interface processes recorded by eclogite-facies shear zones (Monviso, W. Alps). *Lithos*, *127*(1–2), 222–238. https://doi.org/10.1016/j.lithos.2011.09.004

Angiboust, S., Glodny, J., Oncken, O., & Chopin, C. (2014). In search of transient subduction interfaces in the Dent Blanche–Sesia Tectonic System (W. Alps). *Lithos*, *205*, 298–321. https://doi.org/10.1016/j.lithos.2014.07.001

Angiboust, S., Kirsch, J., Oncken, O., Glodny, J., Monié, P., & Rybacki, E. (2015). Probing the transition between seismically coupled and decoupled segments along an ancient subduction interface. *Geochemistry, Geophysics, Geosystems*, *16*(6), 1905–1922. https://doi.org/10.1002/2015gc005776

Angiboust, S., Langdon, R., Agard, P., Waters, D., & Chopin, C. (2012). Eclogitization of the Monviso ophiolite (W. Alps) and implications on subduction dynamics. *Journal of Metamorphic Geology*, *30*(1), 37–61. https://doi.org/10.1111/j.1525-1314.2011.00951.x

Angiboust, S., Wolf, S., Burov, E., Agard, P., & Yamato, P. (2012). Effect of fluid circulation on subduction interface tectonic processes: Insights from thermo-mechanical numerical modelling. *Earth and Planetary Science Letters*, *357*, 238–248. https://doi.org/10.1016/j.epsl.2012.09.012

Arcay, D. (2017). Modelling the interplate domain in thermo-mechanical simulations of subduction: Critical effects of resolution and rheology, and consequences on wet mantle melting. *Physics of the Earth and Planetary Interiors*, *269*, 112–132. https://doi.org/10.1016/j.pepi.2017.05.008

Audet, P., Bostock, M., Christensen, N., & Peacock, S. (2009). Seismic evidence for overpressured subducted oceanic crust and megathrust fault sealing. *Nature*, *457*(7225), 76–78. https://doi.org/10.1038/nature07650

Audet, P., & Kim, Y. (2016). Teleseismic constraints on the geological environment of deep episodic slow earthquakes in subduction zone forearcs: A review. *Tectonophysics*, *670*, 1–15. https://doi.org/10.1016/j.tecto.2016.01.005

Audet, P., & Schaeffer, A. (2018). Fluid pressure and shear zone development over the locked to slow slip region in Cascadia. *Science Advances*, *4*(3), eaar2982. https://doi.org/10.1126/sciadv.aar2982

Avigad, D., & Garfunkel, Z. (1991). Uplift and exhumation of high-pressure metamorphic terrains: The example of the Cycladic blueschist belt (Aegean Sea). *Tectonophysics*, *188*(3–4), 357–372. https://doi.org/10.1016/0040-1951(91)90464-4

Banfield, J., & Raftery, A. (1993). *Model-based Gaussian and non-Gaussian clustering* (pp. 803–821). Biometrics.

Barlow, H. (1989). Unsupervised learning. *Neural Computation*, *1*(3), 295–311. https://doi.org/10.1162/neco.1989.1.3.295

Batchelor, G. (1953). *The theory of homogeneous turbulence*. Cambridge university press.

Baxter, E., & Caddick, M. (2013). Garnet growth as a proxy for progressive subduction zone dehydration. *Geology*, *41*(6), 643–646. https://doi.org/10.1130/g34004.1

Beall, A., Fagereng, Å., & Ellis, S. (2019). Strength of strained two-phase mixtures: Application to rapid creep and stress amplification in subduction zone mélange. *Geophysical Research Letters*, *46*(1), 169–178. https://doi.org/10.1029/2018gl081252

Bebout, G. (2007). Metamorphic chemical geodynamics of subduction zones. *Earth and Planetary Science Letters*, *260*(3–4), 373–393. https://doi.org/10.1016/j.epsl.2007.05.050

Bebout, G., & Barton, M. (2002). Tectonic and metasomatic mixing in a high-t, subduction-zone mélange—Insights into the geochemical evolution of the slab–mantle interface. *Chemical Geology*, *187*(1–2), 79–106. https://doi.org/10.1016/s0009-2541(02)00019-0

Beyssac, O., Goffé, B., Chopin, C., & Rouzaud, J. (2002). Raman spectra of carbonaceous material in metasediments: A new geothermometer. *Journal of Metamorphic Geology*, *20*(9), 859–871. https://doi.org/10.1046/j.1525-1314.2002.00408.x

Bonnet, G., Agard, P., Angiboust, S., Monié, P., Jentzer, M., Omrani, J., et al. (2018). Tectonic slicing and mixing processes along the subduction interface: The Sistan example (Eastern Iran). *Lithos*, *310*, 269–287. https://doi.org/10.1016/j.lithos.2018.04.016

Bostock, M. (2013). The Moho in subduction zones. *Tectonophysics*, *609*, 547–557. https://doi.org/10.1016/j.tecto.2012.07.007

Boussinesq, J. (1897). *Théorie de l'écoulement tourbillonnant et tumultueux des liquides dans les lits rectilignes a grande section* (Vol. 1). Gauthier-Villars.

Bowen, N., & Tuttle, O. (1949). The system $MgO—SiO_2—H_2O$. *Geological Society of America Bulletin*, *60*(3), 439–460. https://doi.org/10.1130/0016-7606(1949)60[439:tsm]2.0.co;2

Burdette, E., & Hirth, G. (2022). Creep rheology of antigorite: Experiments at subduction zone conditions. *Journal of Geophysical Research: Solid Earth*, *127*(7), e2022JB024260. https://doi.org/10.1029/2022jb024260

Burg, J., & Gerya, T. (2005). The role of viscous heating in Barrovian metamorphism of collisional orogens: Thermomechanical models and application to the Lepontine Dome in the Central Alps. *Journal of Metamorphic Geology*, *23*(2), 75–95. https://doi.org/10.1111/j.1525-1314.2005.00563.x

Burov, E., François, T., Agard, P., Le Pourhiet, L., Meyer, B., Tirel, C., et al. (2014). Rheological and geodynamic controls on the mechanisms of subduction and HP/UHP exhumation of crustal rocks during continental collision: Insights from numerical models. *Tectonophysics*, *631*, 212–250. https://doi.org/10.1016/j.tecto.2014.04.033

Calvert, A., Bostock, M., Savard, G., & Unsworth, M. (2020). Cascadia low frequency earthquakes at the base of an overpressured subduction shear zone. *Nature Communications*, *11*(1), 1–10. https://doi.org/10.1038/s41467-020-17609-3

Calvert, A., Preston, L., & Farahbod, A. (2011). Sedimentary underplating at the cascadia mantle-wedge corner revealed by seismic imaging. *Nature Geoscience*, *4*(8), 545–548. https://doi.org/10.1038/ngeo1195

Castro, A., & Spear, F. (2017). Reaction overstepping and re-evaluation of peak P–T conditions of the blueschist unit Sifnos, Greece: Implications for the Cyclades subduction zone. *International Geology Review*, *59*(5–6), 548–562. https://doi.org/10.1080/00206814.2016.1200499

Celeux, G., & Govaert, G. (1995). Gaussian parsimonious clustering models. *Pattern Recognition*, *28*(5), 781–793. https://doi.org/10.1016/0031-3203(94)00125-6

Cisneros, M., Behr, W., Platt, J., & Anczkiewicz, R. (2022). Quartz-in-garnet barometry constraints on formation pressures of eclogites from the Franciscan Complex, California. *Contributions to Mineralogy and Petrology*, *177*(1), 12. https://doi.org/10.1007/s00410-021-01876-4

Cloos, M., & Shreve, R. (1988). Subduction-channel model of prism accretion, melange formation, sediment subduction, and subduction erosion at convergent plate margins: 1. Background and description. *Pure and Applied Geophysics*, *128*(3), 455–500. https://doi.org/10.1007/bf00874548

Connolly, J. (2005). Computation of phase equilibria by linear programming: A tool for geodynamic modeling and its application to subduction zone decarbonation. *Earth and Planetary Science Letters*, *236*(1–2), 524–541. https://doi.org/10.1016/j.epsl.2005.04.033

Currie, C., & Hyndman, R. (2006). The thermal structure of subduction zone back arcs. *Journal of Geophysical Research*, *111*(B8), 1–22. https://doi.org/10.1029/2005jb004024

Currie, C., Wang, K., Hyndman, R., & He, J. (2004). The thermal effects of steady-state slab-driven mantle flow above a subducting plate: The Cascadia subduction zone and backarc. *Earth and Planetary Science Letters*, *223*(1–2), 35–48. https://doi.org/10.1016/j.epsl.2004.04.020

Davies, J. (1999). Simple analytic model for subduction zone thermal structure. *Geophysical Journal International*, *139*(3), 823–828. https://doi.org/10.1046/j.1365-246x.1999.00991.x

Delph, J., Thomas, A., & Levander, A. (2021). Subcretionary tectonics: Linking variability in the expression of subduction along the Cascadia forearc. *Earth and Planetary Science Letters*, *556*, 116724. https://doi.org/10.1016/j.epsl.2020.116724

Dempster, A., Laird, N., & Rubin, D. (1977). Maximum likelihood from incomplete data via the EM algorithm. *Journal of the Royal Statistical Society: Series B*, *39*(1), 1–22. https://doi.org/10.1111/j.2517-6161.1977.tb01600.x

Dragovic, B., Baxter, E., & Caddick, M. (2015). Pulsed dehydration and garnet growth during subduction revealed by zoned garnet geochronology and thermodynamic modeling, Sifnos, Greece. *Earth and Planetary Science Letters*, *413*, 111–122. https://doi.org/10.1016/j.epsl.2014.12.024

England, P., Engdahl, R., & Thatcher, W. (2004). Systematic variation in the depths of slabs beneath arc volcanoes. *Geophysical Journal International*, *156*(2), 377–408. https://doi.org/10.1111/j.1365-246x.2003.02132.x

Faccenda, M. (2014). Water in the slab: A trilogy. *Tectonophysics*, *614*, 1–30. https://doi.org/10.1016/j.tecto.2013.12.020

Faccenda, M., Gerya, T., & Burlini, L. (2009). Deep slab hydration induced by bending-related variations in tectonic pressure. *Nature Geoscience*, *2*(11), 790–793. https://doi.org/10.1038/ngeo656

Faccenda, M., Gerya, T., & Chakraborty, S. (2008). Styles of post-subduction collisional orogeny: Influence of convergence velocity, crustal rheology and radiogenic heat production. *Lithos*, *103*(1–2), 257–287. https://doi.org/10.1016/j.lithos.2007.09.009

Ferris, A., Abers, G., Christensen, D., & Veenstra, E. (2003). High resolution image of the subducted Pacific (?) plate beneath central Alaska, 50–150 km depth. *Earth and Planetary Science Letters*, *214*(3–4), 575–588. https://doi.org/10.1016/s0012-821x(03)00403-5

Ferry, J., & Watson, E. (2007). New thermodynamic models and revised calibrations for the Ti-in-zircon and Zr-in-rutile thermometers. *Contributions to Mineralogy and Petrology*, *154*(4), 429–437. https://doi.org/10.1007/s00410-007-0201-0

Festa, A., Pini, G., Ogata, K., & Dilek, Y. (2019). Diagnostic features and field-criteria in recognition of tectonic, sedimentary and diapiric mélanges in orogenic belts and exhumed subduction-accretion complexes. *Gondwana Research*, *74*, 7–30. https://doi.org/10.1016/j.gr.2019.01.003

Figueiredo, M., & Jain, A. (2002). Unsupervised learning of finite mixture models. *IEEE Transactions on Pattern Analysis and Machine Intelligence*, *24*(3), 381–396. https://doi.org/10.1109/34.990138

Fisher, D., Hooker, J., Smye, A., & Chen, T. (2021). Insights from the geological record of deformation along the subduction interface at depths of seismogenesis. *Geosphere*, *17*(6), 1686–1703. https://doi.org/10.1130/ges02389.1

Fraley, C., & Raftery, A. (2002). Model-based clustering, discriminant analysis, and density estimation. *Journal of the American Statistical Association*, *97*(458), 611–631. https://doi.org/10.1198/016214502760047131

Furukawa, Y. (1993). Depth of the decoupling plate interface and thermal structure under arcs. *Journal of Geophysical Research*, *98*(B11), 20005–20013. https://doi.org/10.1029/93jb02020

Gao, X., & Wang, K. (2014). Strength of stick-slip and creeping subduction megathrusts from heat flow observations. *Science*, *345*(6200), 1038–1041. https://doi.org/10.1126/science.1255487

Gerya, T. (2019). *Introduction to numerical geodynamic modelling*. Cambridge University Press.

Gerya, T., Connolly, J., & Yuen, D. (2008). Why is terrestrial subduction one-sided? *Geology*, *36*(1), 43–46. https://doi.org/10.1130/g24060a.1

Gerya, T., & Stöckhert, B. (2006). Two-dimensional numerical modeling of tectonic and metamorphic histories at active continental margins. *International Journal of Earth Sciences*, *95*(2), 250–274. https://doi.org/10.1007/s00531-005-0035-9

Gerya, T., Stöckhert, B., & Perchuk, A. (2002). Exhumation of high-pressure metamorphic rocks in a subduction channel: A numerical simulation. *Tectonics*, *21*(6), 6-1–6-19. https://doi.org/10.1029/2002tc001406

Gerya, T., & Yuen, D. (2003). Characteristics-based marker-in-cell method with conservative finite-differences schemes for modeling geological flows with strongly variable transport properties. *Physics of the Earth and Planetary Interiors*, *140*(4), 293–318. https://doi.org/10.1016/j.pepi.2003.09.006

Gilio, M., Scambelluri, M., Agostini, S., Godard, M., Pettke, T., Agard, P., et al. (2020). Fingerprinting and relocating tectonic slices along the plate interface: Evidence from the Lago Superiore unit at Monviso (Western Alps). *Lithos*, *352*, 105308. https://doi.org/10.1016/j.lithos.2019.105308

Gorczyk, W., Willner, A., Gerya, T., Connolly, J., & Burg, J. (2007). Physical controls of magmatic productivity at Pacific-type convergent margins: Numerical modelling. *Physics of the Earth and Planetary Interiors*, *163*(1–4), 209–232. https://doi.org/10.1016/j.pepi.2007.05.010

Groppo, C., Rolfo, F., Sachan, H., & Rai, S. (2016). Petrology of blueschist from the Western Himalaya (Ladakh, NW India): Exploring the complex behavior of a lawsonite-bearing system in a paleo-accretionary setting. *Lithos*, *252*, 41–56. https://doi.org/10.1016/j.lithos.2016.02.014

Hacker, B. (1996). Eclogite formation and the rheology, buoyancy, seismicity, and $H_2O$ content of oceanic crust. *Geophysical Monograph-American Geophysical Union*, *96*, 337–346.

Hacker, B. (2008). $H_2O$ subduction beyond arcs. *Geochemistry, Geophysics, Geosystems*, *9*(3). https://doi.org/10.1029/2007gc001707

Hacker, B., Abers, G., & Peacock, S. (2003). Subduction factory 1. Theoretical mineralogy, densities, seismic wave speeds, and $H_2O$ contents. *Journal of Geophysical Research*, *108*(B1), 2029. https://doi.org/10.1029/2001jb001127

Harlow, F. (1962). *The particle-in-cell method for numerical solution of problems in fluid dynamics*. Los Alamos Scientific Laboratory.

Harlow, F. (1964). The particle-in-cell computing method for fluid dynamics. *Methods in Computational Physics*, *3*, 319–343.

Harlow, F., & Welch, J. (1965). Numerical calculation of time-dependent viscous incompressible flow of fluid with free surface. *The Physics of Fluids*, *8*(12), 2182–2189. https://doi.org/10.1063/1.1761178

Harvey, K., Walker, S., Starr, P., Penniston-Dorland, S., Kohn, M., & Baxter, E. (2021). A mélange of subduction ages: Constraints on the timescale of shear zone development and underplating at the subduction interface, Catalina Schist (CA, USA). *Geochemistry, Geophysics, Geosystems*, *22*(9), e2021GC009790. https://doi.org/10.1029/2021gc009790

Hilairet, N., Reynard, B., Wang, Y., Daniel, I., Merkel, S., Nishiyama, N., & Petitgirard, S. (2007). High-pressure creep of serpentine, interseismic deformation, and initiation of subduction. *Science*, *318*(5858), 1910–1913. https://doi.org/10.1126/science.1148494

Holt, A., & Condit, C. (2021). Slab temperature evolution over the lifetime of a subduction zone. *Geochemistry, Geophysics, Geosystems*, *22*(6), e2020GC009476. https://doi.org/10.1029/2020gc009476

Hsü, K. (1968). Principles of mélanges and their bearing on the Franciscan-Knoxville paradox. *Geological Society of America Bulletin*, *79*(8), 1063–1074. https://doi.org/10.1130/0016-7606(1968)79[1063:pomatb]2.0.co;2

Hu, J., & Gurnis, M. (2020). Subduction duration and slab dip. *Geochemistry, Geophysics, Geosystems*, *21*(4), e2019GC008862. https://doi.org/10.1029/2019gc008862

Hyndman, R., Currie, C., & Mazzotti, S. (2005). Subduction zone backarcs, mobile belts, and orogenic heat. *Geological Society of America Today*, *15*(2), 4–10. https://doi.org/10.1130/1052-5173(2005)015<4:szbmba>2.0.co;2

Hyndman, R., & Peacock, S. (2003). Serpentinization of the forearc mantle. *Earth and Planetary Science Letters*, *212*(3–4), 417–432. https://doi.org/10.1016/s0012-821x(03)00263-2

Ioannidi, P., Angiboust, S., Oncken, O., Agard, P., Glodny, J., & Sudo, M. (2020). Deformation along the roof of a fossil subduction interface in the transition zone below seismogenic coupling: The Austroalpine case and new insights from the Malenco Massif (Central Alps). *Geosphere*, *16*(2), 510–532. https://doi.org/10.1130/ges02149.1

Ioannidi, P., Le Pourhiet, L., Agard, P., Angiboust, S., & Oncken, O. (2021). Effective rheology of a two-phase subduction shear zone: Insights from numerical simple shear experiments and implications for subduction zone interfaces. *Earth and Planetary Science Letters*, *566*, 116913. https://doi.org/10.1016/j.epsl.2021.116913

Ito, K., & Kennedy, G. (1971). An experimental study of the basalt-garnet granulite-eclogite transition. *The Structure and Physical Properties of the Earth's Crust*, *14*, 303–314.

Karato, S., & Wu, P. (1993). Rheology of the upper mantle: A synthesis. *Science*, *260*(5109), 771–778. https://doi.org/10.1126/science.260.5109.771

Kerswell, B., Kohn, M., & Gerya, T. (2021). Backarc lithospheric thickness and serpentine stability control slab-mantle coupling depths in subduction zones. *Geochemistry, Geophysics, Geosystems*, *22*(6), e2020GC009304. https://doi.org/10.1029/2020gc009304

Kerswell, B., Kohn, M., & Gerya, T. (2023). Computing rates and distributions of rock recovery in subduction zones [Dataset]. National Science Foundation. https://doi.org/10.17605/OSF.IO/3EMWF

Kitamura, Y., & Kimura, G. (2012). Dynamic role of tectonic mélange during interseismic process of plate boundary mega earthquakes. *Tectonophysics*, *568*, 39–52. https://doi.org/10.1016/j.tecto.2011.07.008

Kohn, M. (2020). A refined zirconium-in-rutile thermometer. *American Mineralogist: Journal of Earth and Planetary Materials*, *105*(6), 963–971. https://doi.org/10.2138/am-2020-7091

Kohn, M., Castro, A., Kerswell, B., Ranero, C. R., & Spear, F. (2018). Shear heating reconciles thermal models with the metamorphic rock record of subduction. *Proceedings of the National Academy of Sciences*, *115*(46), 11706–11711. https://doi.org/10.1073/pnas.1809962115

Kohn, M., & Spear, F. (1991). Error propagation for barometers: 2. Application to rocks. *American Mineralogist*, *76*(1–2), 138–147.

Kotowski, A., & Behr, W. (2019). Length scales and types of heterogeneities along the deep subduction interface: Insights from exhumed rocks on Syros Island, Greece. *Geosphere*, *15*(4), 1038–1065. https://doi.org/10.1130/ges02037.1

Kotowski, A., Cisneros, M., Behr, W., Stockli, D., Soukis, K., Barnes, J., & Ortega-Arroyo, D. (2022). Subduction, underplating, and return flow recorded in the Cycladic Blueschist unit exposed on Syros, Greece. *Tectonics*, *41*(6), e2020TC006528. https://doi.org/10.1029/2020tc006528

Kusky, T., Windley, B., Safonova, I., Wakita, K., Wakabayashi, J., Polat, A., & Santosh, M. (2013). Recognition of ocean plate stratigraphy in accretionary orogens through Earth history: A record of 3.8 billion years of sea floor spreading, subduction, and accretion. *Gondwana Research*, *24*(2), 501–547. https://doi.org/10.1016/j.gr.2013.01.004

Locatelli, M., Federico, L., Agard, P., & Verlaguet, A. (2019). Geology of the southern Monviso metaophiolite complex (W-Alps, Italy). *Journal of Maps*, *15*(2), 283–297. https://doi.org/10.1080/17445647.2019.1592030

Locatelli, M., Verlaguet, A., Agard, P., Federico, L., & Angiboust, S. (2018). Intermediate-depth brecciation along the subduction plate interface (Monviso eclogite, W. Alps). *Lithos*, *320*, 378–402. https://doi.org/10.1016/j.lithos.2018.09.028

Mann, M., Abers, G., Daly, K., & Christensen, D. (2022). Subduction of an oceanic plateau across southcentral Alaska: Scattered-wave imaging. *Journal of Geophysical Research: Solid Earth*, *127*(1), e2021JB022697. https://doi.org/10.1029/2021jb022697

McKenzie, D. (1969). Speculations on the consequences and causes of plate motions. *Geophysical Journal International*, *18*(1), 1–32. https://doi.org/10.1111/j.1365-246x.1969.tb00259.x

Molnar, P., & England, P. (1990). Temperatures, heat flux, and frictional stress near major thrust faults. *Journal of Geophysical Research*, *95*(B4), 4833–4856. https://doi.org/10.1029/jb095ib04p04833

Monié, P., & Agard, P. (2009). Coeval blueschist exhumation along thousands of kilometers: Implications for subduction channel processes. *Geochemistry, Geophysics, Geosystems*, *10*(7), Q07002. https://doi.org/10.1029/2009gc002428

Moresi, L., Dufour, F., & Mühlhaus, H. (2003). A Lagrangian integration point finite element method for large deformation modeling of viscoelastic geomaterials. *Journal of Computational Physics*, *184*(2), 476–497. https://doi.org/10.1016/s0021-9991(02)00031-1

Morishige, M., & Kuwatani, T. (2020). Bayesian inversion of surface heat flow in subduction zones: A framework to refine geodynamic models based on observational constraints. *Geophysical Journal International*, *222*(1), 103–109. https://doi.org/10.1093/gji/ggaa149

Naif, S., Key, K., Constable, S., & Evans, R. (2015). Water-rich bending faults at the Middle America Trench. *Geochemistry, Geophysics, Geosystems*, *16*(8), 2582–2597. https://doi.org/10.1002/2015gc005927

Okay, A. (1989). Alpine-Himalayan blueschists. *Annual Review of Earth and Planetary Sciences*, *17*(1), 55–87. https://doi.org/10.1146/annurev.ea.17.050189.000415

Peacock, S. (1990). Fluid processes in subduction zones. *Science*, *248*(4953), 329–337. https://doi.org/10.1126/science.248.4953.329

Peacock, S. (1996). Thermal and petrologic structure of subduction zones. *Subduction: Top to Bottom*, *96*, 119–133.

Peacock, S., & Hyndman, R. (1999). Hydrous minerals in the mantle wedge and the maximum depth of subduction thrust earthquakes. *Geophysical Research Letters*, *26*(No. 16), 2517–2520. https://doi.org/10.1029/1999gl900558

Peacock, S., & Wang, K. (1999). Seismic consequences of warm versus cool subduction metamorphism: Examples from southwest and northeast Japan. *Science*, *286*(5441), 937–939. https://doi.org/10.1126/science.286.5441.937

Penniston-Dorland, S., & Harvey, K. (2023). Constraints on tectonic processes in subduction mélange: A review of insights from the Catalina Schist (CA, USA). *Geosystems and Geoenvironment*, 100190. https://doi.org/10.1016/j.geogeo.2023.100190

Penniston-Dorland, S., Kohn, M., & Manning, C. (2015). The global range of subduction zone thermal structures from exhumed blueschists and eclogites: Rocks are hotter than models. *Earth and Planetary Science Letters*, *428*, 243–254. https://doi.org/10.1016/j.epsl.2015.07.031

Platt, J. (1975). Metamorphic and deformational processes in the Franciscan Complex, California: Some insights from the Catalina Schist terrane. *Geological Society of America Bulletin*, *86*(10), 1337–1347. https://doi.org/10.1130/0016-7606(1975)86<1337:madpit>2.0.co;2

Platt, J. (1986). Dynamics of orogenic wedges and the uplift of high-pressure metamorphic rocks. *Geological Society of America Bulletin*, *97*(9), 1037–1053. https://doi.org/10.1130/0016-7606(1986)97<1037:doowat>2.0.co;2

Platt, J. (2015). Origin of Franciscan blueschist-bearing mélange at San Simeon, central California coast. *International Geology Review*, *57*(5–8), 843–853. https://doi.org/10.1080/00206814.2014.902756

Plunder, A., Agard, P., Chopin, C., & Okay, A. (2013). Geodynamics of the Tavşanlı zone, western Turkey: Insights into subduction/obduction processes. *Tectonophysics*, *608*, 884–903. https://doi.org/10.1016/j.tecto.2013.07.028

Plunder, A., Agard, P., Chopin, C., Pourteau, A., & Okay, A. (2015). Accretion, underplating and exhumation along a subduction interface: From subduction initiation to continental subduction (Tavşanlı zone, W. Turkey). *Lithos*, *226*, 233–254. https://doi.org/10.1016/j.lithos.2015.01.007

Plunder, A., Thieulot, C., & Van Hinsbergen, D. (2018). The effect of obliquity on temperature in subduction zones: Insights from 3-D numerical modeling. *Solid Earth*, *9*(3), 759–776. https://doi.org/10.5194/se-9-759-2018

Poulaki, E., Stockli, D., & Shuck, B. (2023). Pre-subduction architecture controls coherent underplating during subduction and exhumation (Nevado-Filábride Complex, southern Spain). *Geochemistry, Geophysics, Geosystems*, *24*(3), e2022GC010802. https://doi.org/10.1029/2022gc010802

Ranalli, G. (1995). *Rheology of the Earth*. Springer Science & Business Media.

Reynolds, D. (2009). Gaussian mixture models. *Encyclopedia of Biometrics*, *741*, 659–663.

Roda, M., Marotta, A., & Spalla, M. (2010). Numerical simulations of an ocean-continent convergent system: Influence of subduction geometry and mantle wedge hydration on crustal recycling. *Geochemistry, Geophysics, Geosystems*, *11*(5), Q05008. https://doi.org/10.1029/2009gc003015

Roda, M., Spalla, M., & Marotta, A. (2012). Integration of natural data within a numerical model of ablative subduction: A possible interpretation for the Alpine dynamics of the Austroalpine crust. *Journal of Metamorphic Geology*, *30*(9), 973–996. https://doi.org/10.1111/jmg.12000

Roda, M., Zucali, M., Regorda, A., & Spalla, M. (2020). Formation and evolution of a subduction-related mélange: The example of the Rocca Canavese Thrust Sheets (Western Alps). *Bulletin*, *132*(3–4), 884–896. https://doi.org/10.1130/b35213.1

Rondenay, S., Abers, G., & van Keken, P. (2008). Seismic imaging of subduction zone metamorphism. *Geology*, *36*(4), 275–278. https://doi.org/10.1130/g24112a.1

Ruh, J., Le Pourhiet, L., Agard, P., Burov, E., & Gerya, T. (2015). Tectonic slicing of subducting oceanic crust along plate interfaces: Numerical modeling. *Geochemistry, Geophysics, Geosystems*, *16*(10), 3505–3531. https://doi.org/10.1002/2015gc005998

Schmidt, M., & Poli, S. (1998). Experimentally based water budgets for dehydrating slabs and consequences for arc magma generation. *Earth and Planetary Science Letters*, *163*(1–4), 361–379. https://doi.org/10.1016/s0012-821x(98)00142-3

Schmidt, M., & Poli, S. (2013). Devolatilization during subduction. In *Treatise on geochemistry*, *The crust* (Vol. 4, pp. 669–701). Elsevier.

Schwarz, G. (1978). Estimating the dimension of a model. *Annals of Statistics*, *6*(2), 461–464. https://doi.org/10.1214/aos/1176344136

Scrucca, L., Fop, M., Murphy, T., & Raftery, A. (2016). Mclust 5: Clustering, classification and density estimation using Gaussian finite mixture models. *The R Journal*, *8*(1), 289. https://doi.org/10.32614/rj-2016-021

Shreve, R., & Cloos, M. (1986). Dynamics of sediment subduction, melange formation, and prism accretion. *Journal of Geophysical Research*, *91*(B10), 10229–10245. https://doi.org/10.1029/jb091ib10p10229

Sizova, E., Gerya, T., Brown, M., & Perchuk, L. (2010). Subduction styles in the Precambrian: Insight from numerical experiments. *Lithos*, *116*(3–4), 209–229. https://doi.org/10.1016/j.lithos.2009.05.028

Soret, M., Bonnet, G., Agard, P., Larson, K., Cottle, J., Dubacq, B., et al. (2022). Timescales of subduction initiation and evolution of subduction thermal regimes. *Earth and Planetary Science Letters*, *584*, 117521. https://doi.org/10.1016/j.epsl.2022.117521

Spear, F., & Selverstone, J. (1983). Quantitative PT paths from zoned minerals: Theory and tectonic applications. *Contributions to Mineralogy and Petrology*, *83*(3), 348–357. https://doi.org/10.1007/bf00371203

Spear, F. S. (1993). *Metamorphic phase equilibria and pressure-temperature-time paths* (pp. 352–356). Mineralogical Society of America Monograph.

Stöckhert, B. (2002). Stress and deformation in subduction zones: Insight from the record of exhumed metamorphic rocks. *Geological Society, London, Special Publications*, *200*(1), 255–274. https://doi.org/10.1144/gsl.sp.2001.200.01.15

Syracuse, E., & Abers, G. (2006). Global compilation of variations in slab depth beneath arc volcanoes and implications. *Geochemistry, Geophysics, Geosystems*, *7*(5), Q05017. https://doi.org/10.1029/2005gc001045

Syracuse, E., van Keken, P., Abers, G., Suetsugu, D., Bina, C., Inoue, T., et al. (2010). The global range of subduction zone thermal models. *Physics of the Earth and Planetary Interiors*, *183*(1–2), 73–90. https://doi.org/10.1016/j.pepi.2010.02.004

Tewksbury-Christle, C., & Behr, W. (2021). Constraints from exhumed rocks on the seismic signature of the deep subduction interface. *Geophysical Research Letters*, *48*(18), e2021GL093831. https://doi.org/10.1029/2021gl093831

Tewksbury-Christle, C., Behr, W., & Helper, M. (2021). Tracking deep sediment underplating in a fossil subduction margin: Implications for interface rheology and mass and volatile recycling. *Geochemistry, Geophysics, Geosystems*, *22*(3), e2020GC009463. https://doi.org/10.1029/2020gc009463

Turcotte, D., & Schubert, G. (2002). *Geodynamics*. Cambridge University Press.

van Keken, P., Hacker, B., Syracuse, E., & Abers, G. (2011). Subduction factory: 4. Depth-dependent flux of $H_2O$ from subducting slabs worldwide. *Journal of Geophysical Research*, *116*(B1), b01401. https://doi.org/10.1029/2010jb007922

van Keken, P., Wada, I., Abers, G., Hacker, B., & Wang, K. (2018). Mafic high-pressure rocks are preferentially exhumed from warm subduction settings. *Geochemistry, Geophysics, Geosystems*, *19*(9), 2934–2961. https://doi.org/10.1029/2018gc007624

van Keken, P., Wada, I., Sime, N., & Abers, G. (2019). Thermal structure of the forearc in subduction zones: A comparison of methodologies. *Geochemistry, Geophysics, Geosystems*, *20*(7), 3268–3288. https://doi.org/10.1029/2019gc008334

Vermeesch, P. (2018). IsoplotR: A free and open toolbox for geochronology. *Geoscience Frontiers*, *9*(5), 1479–1493. https://doi.org/10.1016/j.gsf.2018.04.001

Vitale Brovarone, A., & Agard, P. (2013). True metamorphic isograds or tectonically sliced metamorphic sequence? New high-spatial resolution petrological data for the New Caledonia case study. *Contributions to Mineralogy and Petrology*, *166*(2), 451–469. https://doi.org/10.1007/s00410-013-0885-2

Wada, I., & Wang, K. (2009). Common depth of slab-mantle decoupling: Reconciling diversity and uniformity of subduction zones. *Geochemistry, Geophysics, Geosystems*, *10*(10). https://doi.org/10.1029/2009gc002570

Wakabayashi, J. (2015). Anatomy of a subduction complex: Architecture of the Franciscan Complex, California, at multiple length and time scales. *International Geology Review*, *57*(5–8), 669–746. https://doi.org/10.1080/00206814.2014.998728

Wakabayashi, J., & Dilek, Y. (2011). Mélanges of the Franciscan Complex, California: Diverse structural settings, evidence for sedimentary mixing, and their connection to subduction processes. *Mélanges: Processes of Formation and Societal Significance: Geological Society of America Special Paper*, *480*, 117–141.

Yamato, P., Agard, P., Burov, E., Le Pourhiet, L., Jolivet, L., & Tiberi, C. (2007). Burial and exhumation in a subduction wedge: Mutual constraints from thermomechanical modeling and natural P-T-t data (Schistes Lustrés, western Alps). *Journal of Geophysical Research*, *112*(B7), B07410. https://doi.org/10.1029/2006jb004441

Yamato, P., Burov, E., Agard, P., Le Pourhiet, L., & Jolivet, L. (2008). HP-UHP exhumation during slow continental subduction: Self-consistent thermodynamically and thermomechanically coupled model with application to the Western Alps. *Earth and Planetary Science Letters*, *271*(1–4), 63–74. https://doi.org/10.1016/j.epsl.2008.03.049